Centrality dependence of charged hadron and strange hadron elliptic flow from $\sqrt{s_{NN}} = 200$ GeV $Au + Au$ collisions

B.I. Abelev,[10] M.M. Aggarwal,[32] Z. Ahammed,[47] B.D. Anderson,[21] D. Arkhipkin,[14] G.S. Averichev,[13] Y. Bai,[30] J. Balewski,[25] O. Barannikova,[10] L.S. Barnby,[2] J. Baudot,[19] S. Baumgart,[52] D.R. Beavis,[3] R. Bellwied,[50] F. Benedosso,[30] R.R. Betts,[10] S. Bhardwaj,[37] A. Bhasin,[20] A.K. Bhati,[32] H. Bichsel,[49] J. Bielcik,[12] J. Bielcikova,[12] L.C. Bland,[3] M. Bombara,[2] B.E. Bonner,[38] M. Botje,[30] E. Braidot,[30] A.V. Brandin,[28] S. Bueltmann,[3] T.P. Burton,[2] M. Bystersky,[12] X.Z. Cai,[41] H. Caines,[52] M. Calderón de la Barca Sánchez,[6] J. Callner,[10] O. Catu,[52] D. Cebra,[6] M.C. Cervantes,[43] Z. Chajecki,[31] P. Chaloupka,[12] S. Chattopadhyay,[47] H.F. Chen,[40] J.H. Chen,[41] J.Y. Chen,[51] J. Cheng,[45] M. Cherney,[11] A. Chikanian,[52] K.E. Choi,[36] W. Christie,[3] S.U. Chung,[3] R.F. Clarke,[43] M.J.M. Codrington,[43] J.P. Coffin,[19] T.M. Cormier,[50] M.R. Cosentino,[39] J.G. Cramer,[49] H.J. Crawford,[5] D. Das,[6] S. Dash,[16] M. Daugherity,[44] M.M. de Moura,[39] T.G. Dedovich,[13] M. DePhillips,[3] A.A. Derevschikov,[34] R. Derradi de Souza,[8] L. Didenko,[3] T. Dietel,[15] P. Djawotho,[18] S.M. Dogra,[20] X. Dong,[24] J.L. Drachenberg,[43] J.E. Draper,[6] F. Du,[52] J.C. Dunlop,[3] M.R. Dutta Mazumdar,[47] W.R. Edwards,[24] L.G. Efimov,[13] E. Elhalhuli,[2] V. Emelianov,[28] J. Engelage,[5] G. Eppley,[38] B. Erazmus,[42] M. Estienne,[19] L. Eun,[33] P. Fachini,[3] R. Fatemi,[22] J. Fedorisin,[13] A. Feng,[51] P. Filip,[14] E. Finch,[52] V. Fine,[3] Y. Fisyak,[3] C.A. Gagliardi,[43] L. Gaillard,[2] M.S. Ganti,[47] E. Garcia-Solis,[10] V. Ghazikhanian,[7] P. Ghosh,[47] Y.N. Gorbunov,[11] A. Gordon,[3] O. Grebenyuk,[30] D. Grosnick,[46] B. Grube,[36] S.M. Guertin,[7] A. Gupta,[20] N. Gupta,[20] W. Guryn,[3] B. Haag,[6] T.J. Hallman,[3] A. Hamed,[43] J.W. Harris,[52] W. He,[18] M. Heinz,[52] S. Heppelmann,[33] B. Hippolyte,[19] A. Hirsch,[35] A.M. Hoffman,[25] G.W. Hoffmann,[44] D.J. Hofman,[10] R.S. Hollis,[10] H.Z. Huang,[7] E.W. Hughes,[4] T.J. Humanic,[31] G. Igo,[7] A. Iordanova,[10] P. Jacobs,[24] W.W. Jacobs,[18] P. Jakl,[12] F. Jin,[41] P.G. Jones,[2] E.G. Judd,[5] S. Kabana,[42] K. Kajimoto,[44] K. Kang,[45] J. Kapitan,[12] M. Kaplan,[9] D. Keane,[21] A. Kechechyan,[13] D. Kettler,[49] V.Yu. Khodyrev,[34] J. Kiryluk,[24] A. Kisiel,[31] S.R. Klein,[24] A.G. Knospe,[52] A. Kocoloski,[25] D.D. Koetke,[46] T. Kollegger,[15] M. Kopytine,[21] L. Kotchenda,[28] V. Kouchpil,[12] P. Kravtsov,[28] V.I. Kravtsov,[34] K. Krueger,[1] C. Kuhn,[19] A. Kumar,[32] L. Kumar,[32] P. Kurnadi,[7] M.A.C. Lamont,[3] J.M. Landgraf,[3] S. Lange,[15] S. LaPointe,[50] F. Laue,[3] J. Lauret,[3] A. Lebedev,[3] R. Lednicky,[14] C-H. Lee,[36] M.J. LeVine,[3] C. Li,[40] Y. Li,[45] G. Lin,[52] X. Lin,[51] S.J. Lindenbaum,[29] M.A. Lisa,[31] F. Liu,[51] H. Liu,[40] J. Liu,[38] L. Liu,[51] T. Ljubicic,[3] W.J. Llope,[38] R.S. Longacre,[3] W.A. Love,[3] Y. Lu,[40] T. Ludlam,[3] D. Lynn,[3] G.L. Ma,[41] J.G. Ma,[7] Y.G. Ma,[41] D.P. Mahapatra,[16] R. Majka,[52] L.K. Mangotra,[20] R. Manweiler,[46] S. Margetis,[21] C. Markert,[44] H.S. Matis,[24] Yu.A. Matulenko,[34] T.S. McShane,[11] A. Meschanin,[34] J. Millane,[25] M.L. Miller,[25] N.G. Minaev,[34] S. Mioduszewski,[43] A. Mischke,[30] J. Mitchell,[38] B. Mohanty,[47] D.A. Morozov,[34] M.G. Munhoz,[39] B.K. Nandi,[17] C. Nattrass,[52] T.K. Nayak,[47] J.M. Nelson,[2] C. Nepali,[21] P.K. Netrakanti,[35] M.J. Ng,[5] L.V. Nogach,[34] S.B. Nurushev,[34] G. Odyniec,[24] A. Ogawa,[3] H. Okada,[3] V. Okorokov,[28] M. Oldenburg,[24] D. Olson,[24] M. Pachr,[12] S.K. Pal,[47] Y. Panebratsev,[13] T. Pawlak,[48] T. Peitzmann,[30] V. Perevoztchikov,[3] C. Perkins,[5] W. Peryt,[48] S.C. Phatak,[16] M. Planinic,[53] J. Pluta,[48] N. Poljak,[53] N. Porile,[35] A.M. Poskanzer,[24] M. Potekhin,[3] B.V.K.S. Potukuchi,[20] D. Prindle,[49] C. Pruneau,[50] N.K. Pruthi,[32] J. Putschke,[52] I.A. Qattan,[18] R. Raniwala,[37] S. Raniwala,[37] R.L. Ray,[44] D. Relyea,[4] A. Ridiger,[28] H.G. Ritter,[24] J.B. Roberts,[38] O.V. Rogachevskiy,[13] J.L. Romero,[6] A. Rose,[24] C. Roy,[42] L. Ruan,[3] M.J. Russcher,[30] V. Rykov,[21] R. Sahoo,[42] I. Sakrejda,[24] T. Sakuma,[25] S. Salur,[52] J. Sandweiss,[52] M. Sarsour,[43] J. Schambach,[44] R.P. Scharenberg,[35] N. Schmitz,[26] K. Schweda,[24] J. Seger,[11] I. Selyuzhenkov,[50] P. Seyboth,[26] A. Shabetai,[19] E. Shahaliev,[13] M. Shao,[40] M. Sharma,[50] S.S. Shi,[51] X-H. Shi,[41] E.P. Sichtermann,[24] F. Simon,[26] R.N. Singaraju,[47] M.J. Skoby,[35] N. Smirnov,[52] R. Snellings,[30] P. Sorensen,[3] J. Sowinski,[18] H.M. Spinka,[1] B. Srivastava,[35] A. Stadnik,[13] T.D.S. Stanislaus,[46] D. Staszak,[7] R. Stock,[15] M. Strikhanov,[28] B. Stringfellow,[35] A.A.P. Suaide,[39] M.C. Suarez,[10] N.L. Subba,[21] M. Sumbera,[12] X.M. Sun,[24] Z. Sun,[23] B. Surrow,[25] T.J.M. Symons,[24] A. Szanto de Toledo,[39] J. Takahashi,[8] A.H. Tang,[3] Z. Tang,[40] T. Tarnowsky,[35] D. Thein,[44] J.H. Thomas,[24] J. Tian,[41] A.R. Timmins,[2] S. Timoshenko,[28] M. Tokarev,[13] V.N. Tram,[24] A.L. Trattner,[5] S. Trentalange,[7] R.E. Tribble,[43] O.D. Tsai,[7] J. Ulery,[35] T. Ullrich,[3] D.G. Underwood,[1] G. Van Buren,[3] N. van der Kolk,[30] M. van Leeuwen,[30] A.M. Vander Molen,[27] R. Varma,[17] G.M.S. Vasconcelos,[8] I.M. Vasilevski,[14] A.N. Vasiliev,[34] F. Videbaek,[3] S.E. Vigdor,[18] Y.P. Viyogi,[16] S. Vokal,[13] S.A. Voloshin,[50] M. Wada,[44] W.T. Waggoner,[11] F. Wang,[35] G. Wang,[7] J.S. Wang,[23] Q. Wang,[35] X. Wang,[45] X.L. Wang,[40] Y. Wang,[45] J.C. Webb,[46] G.D. Westfall,[27] C. Whitten Jr.,[7] H. Wieman,[24] S.W. Wissink,[18] R. Witt,[52] J. Wu,[40] Y. Wu,[51] N. Xu,[24] Q.H. Xu,[24] Z. Xu,[3] P. Yepes,[38] I-K. Yoo,[36] Q. Yue,[45] M. Zawisza,[48] H. Zbroszczyk,[48] W. Zhan,[23] H. Zhang,[3] S. Zhang,[41] W.M. Zhang,[21] Y. Zhang,[40] Z.P. Zhang,[40] Y. Zhao,[40] C. Zhong,[41] J. Zhou,[38] R. Zoulkarneev,[14] Y. Zoulkarneeva,[14] and J.X. Zuo[41]

(STAR Collaboration)

[1]Argonne National Laboratory, Argonne, Illinois 60439
[2]University of Birmingham, Birmingham, United Kingdom
[3]Brookhaven National Laboratory, Upton, New York 11973
[4]California Institute of Technology, Pasadena, California 91125
[5]University of California, Berkeley, California 94720
[6]University of California, Davis, California 95616
[7]University of California, Los Angeles, California 90095
[8]Universidade Estadual de Campinas, Sao Paulo, Brazil
[9]Carnegie Mellon University, Pittsburgh, Pennsylvania 15213
[10]University of Illinois at Chicago, Chicago, Illinois 60607
[11]Creighton University, Omaha, Nebraska 68178
[12]Nuclear Physics Institute AS CR, 250 68 Řež/Prague, Czech Republic
[13]Laboratory for High Energy (JINR), Dubna, Russia
[14]Particle Physics Laboratory (JINR), Dubna, Russia
[15]University of Frankfurt, Frankfurt, Germany
[16]Institute of Physics, Bhubaneswar 751005, India
[17]Indian Institute of Technology, Mumbai, India
[18]Indiana University, Bloomington, Indiana 47408
[19]Institut de Recherches Subatomiques, Strasbourg, France
[20]University of Jammu, Jammu 180001, India
[21]Kent State University, Kent, Ohio 44242
[22]University of Kentucky, Lexington, Kentucky, 40506-0055
[23]Institute of Modern Physics, Lanzhou, China
[24]Lawrence Berkeley National Laboratory, Berkeley, California 94720
[25]Massachusetts Institute of Technology, Cambridge, MA 02139-4307
[26]Max-Planck-Institut für Physik, Munich, Germany
[27]Michigan State University, East Lansing, Michigan 48824
[28]Moscow Engineering Physics Institute, Moscow Russia
[29]City College of New York, New York City, New York 10031
[30]NIKHEF and Utrecht University, Amsterdam, The Netherlands
[31]Ohio State University, Columbus, Ohio 43210
[32]Panjab University, Chandigarh 160014, India
[33]Pennsylvania State University, University Park, Pennsylvania 16802
[34]Institute of High Energy Physics, Protvino, Russia
[35]Purdue University, West Lafayette, Indiana 47907
[36]Pusan National University, Pusan, Republic of Korea
[37]University of Rajasthan, Jaipur 302004, India
[38]Rice University, Houston, Texas 77251
[39]Universidade de Sao Paulo, Sao Paulo, Brazil
[40]University of Science & Technology of China, Hefei 230026, China
[41]Shanghai Institute of Applied Physics, Shanghai 201800, China
[42]SUBATECH, Nantes, France
[43]Texas A&M University, College Station, Texas 77843
[44]University of Texas, Austin, Texas 78712
[45]Tsinghua University, Beijing 100084, China
[46]Valparaiso University, Valparaiso, Indiana 46383
[47]Variable Energy Cyclotron Centre, Kolkata 700064, India
[48]Warsaw University of Technology, Warsaw, Poland
[49]University of Washington, Seattle, Washington 98195
[50]Wayne State University, Detroit, Michigan 48201
[51]Institute of Particle Physics, CCNU (HZNU), Wuhan 430079, China
[52]Yale University, New Haven, Connecticut 06520
[53]University of Zagreb, Zagreb, HR-10002, Croatia

(Dated: April 18, 2008)

We present STAR results on the elliptic flow v_2 of charged hadrons, strange and multi-strange particles from $\sqrt{s_{NN}} = 200$ GeV $Au + Au$ collisions at RHIC. The detailed study of the centrality dependence of v_2 over a broad transverse momentum range is presented. Comparison of different analysis methods are made in order to estimate systematic uncertainties. In order to discuss the non-flow effect, we have performed the first analysis of v_2 with the Lee-Yang Zero method for K^0_S and Λ .

In the relatively low p_T region, $p_T \leq 2$ GeV/c, a scaling with $m_T - m$ is observed for identified hadrons in each centrality bin studied. However, we do not observe $v_2(p_T)$ scaled by the participant eccentricity to be independent of centrality. At higher p_T , 2 GeV/c $\leq p_T \leq 6$ GeV/c, v_2 scales

with quark number for all hadrons studied. For the multi-strange hadron Ω, which does not suffer appreciable hadronic interactions, the values of v_2 are consistent with both $m_T - m$ scaling at low p_T and number-of-quark scaling at intermediate p_T. As a function of collision centrality, an increase of p_T-integrated v_2 scaled by the participant eccentricity has been observed, indicating a stronger collective flow in more central $Au + Au$ collisions.

PACS numbers: 25.75.Ld, 25.75.Dw

I. INTRODUCTION

The event azimuthal anisotropy with respect to the reaction plane has been widely studied in order to evaluate the collective behavior of the matter produced in high-energy nuclear collisions [1, 2, 3]. The initial configuration space anisotropy is expected to be self-quenched by expansion and reduced by frequent re-scatterings in the hot and dense medium created in such collisions. The final observed momentum space anisotropies, therefore, carry information about the early stage collision dynamics [4, 5, 6]. The experimental results of the second harmonic azimuthal anisotropy, elliptic flow, v_2, from $Au + Au$ collisions have demonstrated the development of partonic collectivity [7, 8, 9, 10]. Further detailed analyses of the hadron mass dependence of v_2 suggest that the system has been in the deconfined state with constituent quark degrees of freedom prior to hadronization [11, 12, 13]. Furthermore, results of multi-strange hadron transverse momentum distributions and v_2 indicate that the system reached thermalization at the partonic stage [14, 15, 16, 17].

Hydrodynamic model calculations, with the assumption of ideal fluid behavior (no viscosity), have been successful when compared with the experimental data at RHIC [6, 8, 11, 18]. It should be noted that up to now, the discussions of the underlying dynamics of the thermalization at RHIC are inconclusive. Some initial evidence for thermalization was provided by the quantitative agreement of v_2 results between ideal hydrodynamic model calculations and data for identified hadrons π, K, p and Λ [11, 19] from *minimum bias* (0 - 80% centrality) $Au + Au$ collisions [20]. As shown in Refs. [7, 8], ideal hydrodynamic model calculations have failed to reproduce the centrality dependence of π and p v_2 in $Au + Au$ collisions. In addition, the discussion based on the integrated v_2/ε_{part} of charged hadrons suggests possible thermalization *only* for the most central collisions at RHIC (see Refs. [21, 22] and references therein). Here the participant eccentricity, ε_{part}, is the initial configuration space eccentricity of the participants. From peripheral to the most central $Au + Au$ collisions, the values of v_2/ε_{part} increase as a function of the scaled charged hadron multiplicity, as predicted by a model calculation assuming the *low density limit* [23] of single forward nucleon-nucleon collisions. This analysis indicates that the system has probably not reached thermalization for most peripheral $Au+Au$ collisions.

Hydrodynamic model calculations predict a characteristic dependence of the elliptic flow and transverse momentum spectra on particle mass and collision centrality. Nevertheless the comparisons made so far have been mostly restricted to identified hadrons from minimum bias collisions or integrated v_2 of charged hadrons [21]. Systematic comparisons for identified hadrons at different collision centralities are still scarce [8]. In order to fill this gap and further advance our understanding of the properties of the medium created in high-energy nuclear collisions, in this article we report the centrality dependence of the azimuthal anisotropy parameter v_2 (elliptic flow) in $\sqrt{s_{NN}}$ = 200 GeV $Au + Au$ collisions. The centrality dependence of v_2 for identified hadrons K^0_S, Λ, Ξ, and Ω, and the scaling properties as a function of number of quarks within a given hadron and the transverse kinetic energy $m_T - m$ are reported. Results from the Lee-Yang Zero method [24, 25] for unidentified charged hadrons ($h^+ + h^-$), K^0_S and Λ are also reported. In complex nuclear collisions different systematic errors on v_2 can arise from different analysis methods. In this paper, the systematic errors are analyzed by comparing the standard event plane method [2, 8] with results from the Lee-Yang Zero [25], four-particle cumulant [22, 26], and η subevent [8] methods.

The paper is organized in the following way: we discuss experimental cuts, data selections and methods used for unidentified charged hadrons and identified hadrons in Section II. Section III gives the results on v_2 for unidentified charged hadrons and identified hadrons along with a discussion of the systematic errors extracted from different analysis methods. Section IV presents a comparison with model calculations as well as a discussion of scaling and the systematics of the $v_2(p_T)$ distributions from SPS ($\sqrt{s_{NN}}$= 17.3 GeV) and RHIC ($\sqrt{s_{NN}}$= 62.4 and 200 GeV). Finally, the summary of the analysis and the outlook are presented in Section V.

II. METHODS AND ANALYSIS

In this paper, if v_2 is used without curly brackets it is an abbreviation for $v_2\{EP_2\}$, that is, v_2 relative to the second harmonic event plane. The systematic uncertainty from the event plane resolution is constant at each centrality and

expected to be smaller than that of the observed differential flow, and is not folded in. Other systematic errors are discussed in Section III.

A. Data sets

For this study, the high statistics data from $\sqrt{s_{NN}} = 200$ GeV $Au+Au$ collisions collected by the STAR experiment during RHIC's fourth year (2004) of data taking were analyzed. STAR's main time projection chamber (TPC) [27] was used for tracking and identification of charged particles. The TPC records the hits used for reconstructions of the tracks of the particles, enabling the measurement of the momenta of the particles, and identifying the particles by measuring their ionization energy loss. The TPC provides complete azimuthal coverage and complete tracking for charged particles within ± 1.8 units of pseudorapidity. The two forward time projection chambers (FTPC) cover two sides of the collision with $2.5 < \mid \eta \mid < 4.0$. The FTPCs also provide a tool for studying non-flow effects. About 25 million minimum bias events (0–80% most central of the hadronic interaction cross section) were analyzed, which increased the statistics for flow analysis by more than a factor of 10 compared to the previous measurements [8, 10, 12].

The centrality definition of an event was based on the number of charged tracks in the TPC with track quality cuts, which are $|\eta| < 0.5$, a distance of closest approach to the primary vertex (DCA) less than 3 cm, and fit points more than 15. These events were grouped into three centrality bins, which were central (0–10%), mid-central (10–40%), and peripheral (40–80%). In addition, the central dataset (0–10%) was enhanced by online triggering on the most central events with the Zero-Degree Calorimeter (ZDC) [28], thereby getting an additional ∼19 million events for a similar centrality bin. Within the statistical uncertainty, the results from the central trigger dataset were consistent with those from the minimum bias trigger.

The analyzed charged particles were identified as the track helix in the TPC magnetic field. The charged tracks were selected with a transverse momentum range of $0.15 < p_T < 2.0$ GeV/c unless indicated otherwise, and a pseudorapidity range of $\mid \eta \mid < 1.0$. For the Lee-Yang Zero product generating function analysis the η interval increased to $\mid \eta \mid < 1.3$ in order to obtain more particles. A minimum of 15 track fit hits and a ratio of hits to maximum possible hits > 0.52 was also required. To improve the selection of good tracks from the primary collisions, the distance of closest approach of the analyzed tracks to the event vertex had to be less than 2 cm. Tracks of charged daughter particles stemming from weak decay, which tend to be at large distances, are not subject to this cut.

B. Particle identification

We identified K^0_S , Λ ($\overline{\Lambda}$), Ξ^- ($\overline{\Xi}^+$), Ω^- ($\overline{\Omega}^+$) through their decay channel: $K^0_S \to \pi^+ + \pi^-$, $\Lambda \to p + \pi^-$ ($\overline{\Lambda} \to \overline{p} + \pi^+$), $\Xi^- \to \Lambda + \pi^-$ ($\overline{\Xi}^+ \to \overline{\Lambda} + \pi^+$), $\Omega^- \to \Lambda + K^-$ ($\overline{\Omega}^+ \to \overline{\Lambda} + K^+$). The charged pions, kaons and protons were identified via their energy loss in the TPC [27]. According to the (multi)strange particle decay properties, topological cuts and kinematic cuts were applied to reduce the combinatorial background. The detailed description of the analysis method can be found in Refs [10, 29] for K^0_S and Λ , and Refs. [12, 30] for Ξ and Ω.

Figure 1 shows the invariant mass distributions for (a1) K^0_S , (b1) $\Lambda + \overline{\Lambda}$, (c1) $\Xi^- + \overline{\Xi}^+$ and (d1) $\Omega^- + \overline{\Omega}^+$ for a given p_T bin from $\sqrt{s_{NN}} = 200$ GeV minimum bias (0–80%) $Au + Au$ collisions. Clear signal peaks are seen at the values expected for the particle mass above the combinatorial background. The measured invariant mass distributions contain both signal (Sig) and combinatorial background (Bg). For K^0_S and Λ , the measured invariant mass distributions were fitted by a polynomial (up to 4^{th} order), which represents the background, and a double-Gaussian function, which represents the signal. The double-Gaussian was used because of tails on the distribution. For multi-strange baryons Ξ and Ω, the Bg was estimated by rotating the transverse momentum of the daughter Λ by 180°. This operation breaks the correlation between the Λ and the other daughter particle. The resulting invariant mass distributions provide a good approximation for the true background distribution. The detailed description of the method can be found in Ref. [12].

For v_2 of the identified particles, K^0_S , $\Lambda + \overline{\Lambda}$, $\Xi^- + \overline{\Xi}^+$ and $\Omega^- + \overline{\Omega}^+$, the v_2 versus m_{inv} method is used in this analysis [31]. Since v_2 is additive, one can write the total v_2^{Sig+Bg} as a sum of Sig and Bg contributions weighted by their relative yields:

$$v_2^{Sig+Bg}(m_{inv}) = v_2^{Sig} \cdot \frac{Sig}{Sig+Bg}(m_{inv}) \; + \; v_2^{Bg}(m_{inv}) \cdot \frac{Bg}{Sig+Bg}(m_{inv}). \tag{1}$$

This method involves the calculation of v_2^{Sig+Bg} as a function of m_{inv} and then fitting the distribution using Eq. (1) with measured relative yields and parameterizations of v_2^{Sig} and $v_2^{Bg}(m_{inv})$. The $\frac{Bg}{Sig+Bg}(m_{inv})$ distribution is the

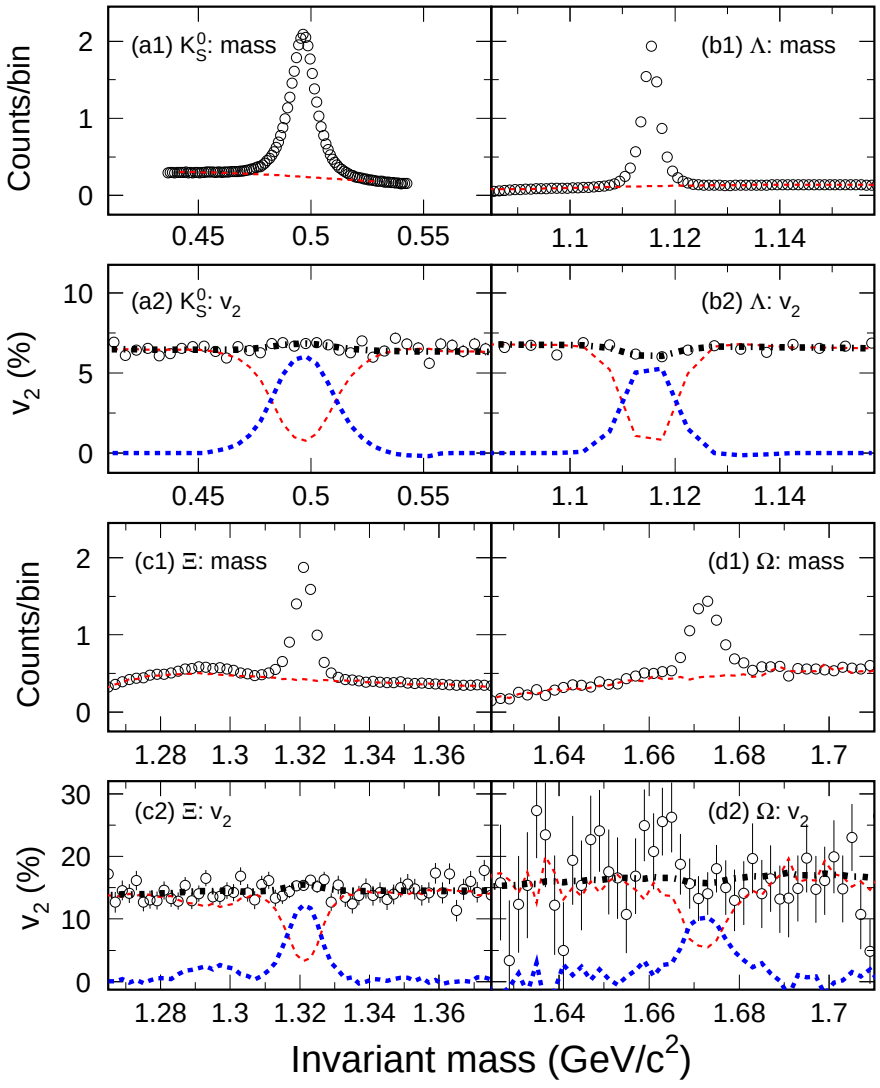

FIG. 1: (Color online) Plots (a1)–(d1) represent the invariant mass distributions for K^0_S ($1.4 \leq p_T \leq 1.6$ GeV/c), Λ ($1.4 \leq p_T \leq 1.6$ GeV/c), Ξ ($2.3 \leq p_T \leq 2.6$ GeV/c), and Ω ($2.5 \leq p_T \leq 3.0$ GeV/c), respectively, from $\sqrt{s_{NN}}$= 200 GeV minimum bias (0–80%) $Au+Au$ collisions. The dashed lines are the background distributions. The corresponding data for the v_2 distributions are shown in plots (a2)–(d2) as open circles. The thick-dashed, thin-dashed and the dot-dashed lines represent the relative contributions of $v_2(Sig)$, $v_2(Bg)$, and $v_2(Sig+Bg)$, respectively. For clarity, the invariant mass plots for K^0_S, Λ, Ξ, and Ω, are scaled by 1/50000, 1/170000, 1/2.5, and 1/3, respectively. The error bars are shown only for the statistical uncertainties.

Bg divided by $(Sig+Bg)$. The $\frac{Sig}{Sig+Bg}(m_{inv})$ distribution is simply calculated by $1 - \frac{Bg}{Sig+Bg}(m_{inv})$. The term $v_2^{Bg}(m_{inv})$ is parameterized as a linear function in order to take care of the non-constant v_2^{Bg} value as a function of m_{inv}. The fit result v_2^{Sig} is the final observed v_2. The fit results for K^0_S , $\Lambda + \overline{\Lambda}$, $\Xi^- + \overline{\Xi}^+$ and $\Omega^- + \overline{\Omega}^+$ are shown, as dot-dashed lines, in Fig. 1 (a2), (b2), (c2), and (d2), respectively. Note that the anisotropy varies as a function of p_T and hadron mass. In this figure, the v_2 are shown for different hadrons with the p_T cuts that are listed in the caption. How this method works well for measuring signal v_2 is explained as following: a set of data points are used in the fit over a wide m_{inv} region for Sig and Bg. Data points far from the mass peak constrain $v_2^{Bg}(m_{inv})$ since pure Bg is expected in this region. (The disagreement at $M_{inv} \sim 1.29\,\mathrm{GeV}/c^2$ in (c1) is caused by mis-identified hadrons in the Lambda-pion combinations, which is explained in Ref. [12].) Under the peak, the $v_2^{Sig+Bg}(m_{inv})$ is dominated by the Sig distribution. Finally, the v_2 signal is extracted by the fitting method shown in Eq. 1.

The results obtained with this technique are in good agreement with the ones from the method used previously [2]. Note that the subtraction procedure used to extract the v_2 signal for a given identified particle is independent of the flow correlations. The v_2 distributions of the overall signal and background are evaluated by a specific flow analysis

method. These methods will be discussed in Section II C.

C. Flow analysis methods

The systematic uncertainty of the Event Plane method is evaluated by comparing the results to those obtained by other techniques for measuring anisotropic flow. The various methods have different sensitivities to non-flow effects and v_2 fluctuations, and such studies provide information on the magnitude of the systematic uncertainty. Non-flow effects are correlations not associated with the reaction plane, and include resonance decays, HBT correlations, final state interactions, and jets, to the extent that they do not participate in the flow.

1. Event Plane method

The essence of the Event Plane method [2] is to first estimate the reaction plane. The estimated reaction plane is called the event plane and is determined by the anisotropic flow itself for each harmonic of the Fourier expansion of the anisotropic flow. The event flow vector Q_2 and the event plane angle Ψ_2 are defined by the following equations:

$$Q_2 \cos(2\Psi_2) \;=\; Q_{2x} \;=\; \sum_i w_i \cos(2\phi_i) \tag{2}$$

$$Q_2 \sin(2\Psi_2) \;=\; Q_{2y} \;=\; \sum_i w_i \sin(2\phi_i) \tag{3}$$

$$\Psi_2 \;=\; \left(\tan^{-1}\frac{Q_{2y}}{Q_{2x}}\right)/2 \tag{4}$$

where the sum goes over all the particles i used in the event plane calculation. ϕ_i and w_i are the lab azimuthal angle and the weight for the particle i, respectively. In this analysis, the weights are taken to be the value of p_T in GeV/c up to 2 GeV/c and then constant at 2.0 above that p_T .

The observed v_2 is the second harmonic of the azimuthal distribution of particles with respect to this event plane:

$$v_2^{obs} \;=\; \langle \cos[2(\phi - \Psi_2)] \rangle \tag{5}$$

where angle brackets denote an average over all particles with their azimuthal angle ϕ in a given phase space. Since finite multiplicity limits the resolution in estimating the angle of the reaction plane, the real v_2 has to be corrected for the event plane resolution by

$$v_2 \;=\; \frac{v_2^{obs}}{\langle \cos[2(\Psi_2 - \Psi_r)] \rangle} \tag{6}$$

where brackets denote an average over a large event sample, and Ψ_r is the angle of the reaction plane. The event plane resolution is estimated by the correlation of the event planes of two subevents. The event plane resolution for the subevents with the assumption of pure flow correlations between the subevents is

$$\langle \cos[2(\Psi_2^A - \Psi_r)] \rangle = \sqrt{\langle \cos[2(\Psi_2^A - \Psi_2^B)] \rangle} \tag{7}$$

where A and B denote two subgroups of tracks. In this analysis, we use two random subevents with equal numbers of particles. Further, the full event plane resolution is obtained from the resolution of the subevents:

$$\langle \cos[2(\Psi_2 - \Psi_r)] \rangle = C \langle \cos[2(\Psi_2^A - \Psi_r)] \rangle \tag{8}$$

where C is a constant calculated from the known multiplicity dependence of the resolution [2]. In the case of low resolution (< 0.5), C is equal to $\sqrt{2}$ [2]. The actual event plane resolutions, for the centrality bins used in this analysis of 0-10%, 10-40% and 40-80%, were 0.658 $\pm$ 0.0006, 0.818 $\pm$ 0.0002 and 0.694 $\pm$ 0.0004, respectively.

2. η-subevent method

The η-subevent method attempts to reduce the contribution from non-flow effects (mostly due to short range correlations) by correlating particles separated in pseudorapidity. This technique is similar to the event plane method, except one defines the event flow vector for each particle based on particles measured in the opposite hemisphere in pseudorapidity:

$$v_2\{\eta_\pm\} = \frac{\left\langle \cos[2(\phi_{\eta_\pm} - \Psi_{2,\eta_\mp})] \right\rangle}{\sqrt{\left\langle \cos[2(\Psi_{2,\eta_+} - \Psi_{2,\eta_-})] \right\rangle}}. \tag{9}$$

Here Ψ_{2,η_+} (Ψ_{2,η_-}) is the second harmonic event plane angle defined for particles with positive (negative) pseudorapidity. An η gap of $\mid \eta \mid \; < 0.075$ between positive and negative pseudorapidity subevents is introduced in order to guarantee that non-flow effects are reduced by enlarging the separation between the correlated particles. In Eq. (9) the non-flow effects (correlations) are reduced in both the observed flow (numerator) and the event plane resolution (denominator). Depending on the nature of the remaining non-flow effects, v_2 measured this way may have values which are either lower or higher than those obtained with the standard method.

3. 4-particle cumulant method

A method to calculate v_2 from true four-particle correlations was developed in Ref. [26] and it has already been used by STAR [22]. It uses the cumulant relation

$$C\{4\} \equiv \left\langle u_{n,1} u_{n,2} u^*_{n,3} u^*_{n,4} \right\rangle - 2 \left\langle u_{n,1} u^*_{n,2} \right\rangle^2 = -v_n^4\{4\}\,, \tag{10}$$

where $u_{n,j} = e^{in\phi_j}$. The cumulant allows one to subtract the two-particle correlations, including two-particle non-flow, from the four-particle correlations. In practice, cumulants are calculated using the generating function from Ref. [26] and described in Ref. [22]:

$$G_n(z) = \prod_{j=1}^{M} \left(1 + \frac{z^* u_{n,j} + z u^*_{n,j}}{M}\right), \tag{11}$$

where $z \equiv |z| e^{i\alpha}$ is an arbitrary complex number, with z^* denoting its complex conjugate. The cumulants are related to the generating function by

$$M \cdot \left(\langle G_n(z) \rangle^{1/M} - 1 \right) = \sum_k \frac{|z|^{2k}}{(k!)^2} C\{2k\}\,. \tag{12}$$

The fit to the $C\{4\}$ term is needed. The fourth root of the negative of it gives $v_2\{4\}$.

4. Lee-Yang Zero method

The Lee-Yang Zero method [24, 25] is based on a 1952 proposal of Lee and Yang to detect a liquid-gas phase transition. As opposed to the four-particle cumulant method which is sensitive to the correlations of four particles, this method is sensitive to the correlations of all the particles. Thus it is supposed to remove non-flow correlations to all orders. It has so far been used only to analyze one set of experimental data [32] and one set of transport calculations [33]. The method utilizes the second-harmonic flow vector, Q_2, projected on to an arbitrary laboratory angle, θ:

$$Q_2^\theta = \sum_{j=1}^{M} w_j \cos(2(\phi_j - \theta)), \tag{13}$$

where the sum is taken over all the particles j with lab angles ϕ_j and weights w_j. For this method the weights are taken to be the value of p_T in GeV/c for unidentified charged hadrons and 1.0 for identified particles. We have taken five equally spaced values of θ to average out detector acceptance effects. The results were not different when 20

values of θ were used. The theory of the method [24] is to find a zero of a complex generating function, but in practice the first minimum of the modulus of the generating function along the imaginary axis is used. The sum generating function based on Q_2^θ is given by

$$G_2^\theta(ir) = \mid \langle e^{irQ_2^\theta} \rangle \mid, \tag{14}$$

where r is a variable along the imaginary axis of the complex plane and the average is taken over all events. When data are analyzed in small batches, the $G_2^\theta(ir)$ histograms are combined before finding the first minimum. Such a histogram is shown in Fig. 2(a). The square of the modulus is used to determine the first minimum. The position along the imaginary axis of the first minimum of the modulus of the generating function at the lab angle θ is called r_0^θ, and is related to the "integrated" flow by

$$V_2^\theta = j_{01}/r_0^\theta \tag{15}$$

$$v_2 = \left\langle V_2^\theta \right\rangle_\theta / M, \tag{16}$$

where $j_{01} = 2.405$ is the first root of the Bessel Function J_0 and M is the multiplicity. In the second equation the average is taken over the lab angles θ. However, Eq. (16) is only valid for unit weights. Normally, the anisotropic flow parameter averaged over p_T and η is obtained by taking the yield-weighted average of the differential flow. For unit weights this has been shown to agree with the "integrated" flow from Eq. (16). The differential flow obtained by a second pass through the data is given by

$$\begin{aligned} v_{2m}^\theta(\eta, p_T) &= V_2^\theta \frac{J_1(j_{01})}{J_m(j_{01})} \mathbf{Re}\left(\frac{\left\langle \cos[2m(\phi_j - \theta)] e^{ir_0^\theta Q_2^\theta} \right\rangle}{i^{m-1} \left\langle Q_2^\theta e^{ir_0^\theta Q_2^\theta} \right\rangle} \right), \\ v_{2m}(\eta, p_T) &= \left\langle v_{2m}^\theta(\eta, p_T) \right\rangle_\theta \end{aligned} \tag{17}$$

where $m = 1$ for v_2 and $m = 2$ for v_4. The average in the numerator in the first equation is over the particles of interest and the average in the denominator is over all events.

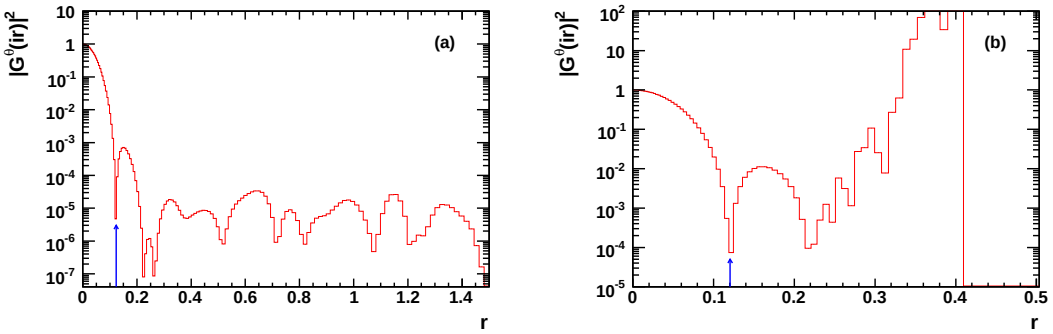

FIG. 2: (Color online) Examples of the modulus of the second harmonic Lee-Yang Zero Generating Functions plotted as a function of the imaginary axis coordinate, r. The Sum Generating Function is shown in (a) and the Product Generating Function in (b). The vertical arrows indicate the positions of the first minimum, called r_0. Note that in (b) the horizontal scale does not go out as far because the calculations were terminated. All data are from $\sqrt{s_{NN}}$= 200 GeV $Au + Au$ collisions.

The product generating function is

$$G_2^\theta(ir) = \mid \langle \prod_{j=1}^{M} [1 + irw_j \cos(2(\phi_j - \theta))] \rangle \mid . \tag{18}$$

This takes more computer time because the product over all particles has to be calculated for each value of r. An example is shown in Fig. 2(b). It can be seen that the sum generating function oscillates after the first minimum, but the product generating function rises very fast. Thus, for the product generating function, the calculation was halted when $|G_2^\theta(ir)|^2$ got larger than 1000. This happened at various r values between 0.2 and 0.4. While the method using

the sum generating function is slightly faster than the standard method [2], using the product generating function is about four times slower. For the product generating function, Eqs. (15, 16) still hold, but the differential flow is given by

$$v_{2m}^{\theta}(\eta, p_T) = V_2^{\theta} \frac{J_1(j_{01})}{J_m(j_{01})} \mathbf{Re} \left(\frac{\left\langle G_2^{\theta}(ir_0^{\theta}) \frac{\cos(2m(\phi_j - \theta))}{1 + ir_0^{\theta} w_j \cos(2(\phi_j - \theta))} \right\rangle}{i^{m-1} \left\langle G_2^{\theta}(ir_0^{\theta}) \sum_j \frac{w_j \cos(2(\phi_j - \theta))}{1 + ir_0^{\theta} w_j \cos(2(\phi_j - \theta))} \right\rangle} \right), \tag{19}$$

where again the average in the numerator is over the particles of interest and the average in the denominator is over all events. Although the sum generating function works fine for v_2, analyses for v_4 (and v_1) have to be based on the product generating function [25]. This is because the product generating function is better at suppressing autocorrelation effects which are more important for mixed harmonics. All methods used in this paper have been tested on simulated data. Also, since drift of the beam in the detector over time might simulate the effect of anisotropic flow, run-by-run recentering of the Q vector was applied, but produced no improvement in the results.

The errors were calculated from the variation of the results for different event sub-samples. For very large errors this technique could underestimate the error because even when there is no flow the method will find a minimum from a fluctuation. In fact the Lee-Yang Zero method only works for sufficient signal-to-noise ratio. Since the signal is v_2 and the noise is proportional to $1/\sqrt{M}$, the parameter $\chi = v_2\sqrt{M}$ determines the applicability of the method. We find that the errors get large and the results scatter when $\chi < 0.8$, and thus the results are presented here only for 10–50% centrality. The method fails for more central collisions because v_2 is small, and for more peripheral collisions because the multiplicity is small.

III. RESULTS

A. Charged hadrons

To evaluate the different flow analysis methods and to estimate systematic uncertainties, charged hadrons were analyzed first. Figure 3 shows $v_2(\eta)$ for both the Lee-Yang Zero and Event-Plane methods. For the Event-Plane method, the event plane was taken from the main TPC, both for tracks in the TPC as well as the FTPC. For the Lee-Yang Zero method, where there is no event plane, tracks in all three TPCs were used. The Lee-Yang Zero results are for the product generating function but are in agreement with the sum generating function results. Elliptic flow falls off in the Forward TPC (FTPC) covering $\mid \eta \mid$ from 2.6 to 4.2. This fall off is probably because the spectra as a function of p_T are steeper at high η and give less weight to the large v_2 values at high p_T [34]. Agreement in the FTPC region between two-particle and multiparticle methods has been seen previously [8]. Having a gap in pseudorapidity between the particles being correlated reduces the non-flow effects due to short range correlations. Indeed, PHOBOS correlates particles with an event plane from a different part of their detector, which is essentially similar to the η-subevent method. With $\mid \eta \mid \leq 1$, PHOBOS [35] data points are consistent with STAR Lee-Yang Zero data although it appears that PHOBOS data may be more peaked. Averaging over the TPC η region $\mid \eta \mid \ < 1.0$, the $v_2(p_T)$ values are shown in Fig. 4 (a) together with Event-Plane and 4-particle cumulant results. For these charged hadrons, the ratio of the four-particle cumulant result to the Event-Plane method shown in Fig. 4 (b) falls off as p_T increases. This indicates a non-flow effect in the Event-Plane method which increases with p_T as one would expect for the contribution of jets. On the other hand, the Lee-Yang Zero ratio seems to be flat. Figure 5 (a) shows the integrated v_2 (averaged over η and p_T) for four different analysis methods as a function of centrality. The ratios to the Event-Plane method are shown in Fig. 5 (b). The centrality region where all methods have reasonable error bars is 10 to 50%. The Event-Plane method appears to be about 15% higher compared to the other methods known to greatly reduce non-flow effects. This effect was already seen in the differential data as a function of η for $p_T < 2$ GeV/c in Fig. 3 and as a function of p_T in Fig. 4. For the most peripheral collisions non-flow might be larger and for the most central collisions fluctuations could be important. From Fig. 5 we would estimate the systematic errors at these other centralities to be 20%, and also probably this same value for minimum bias events.

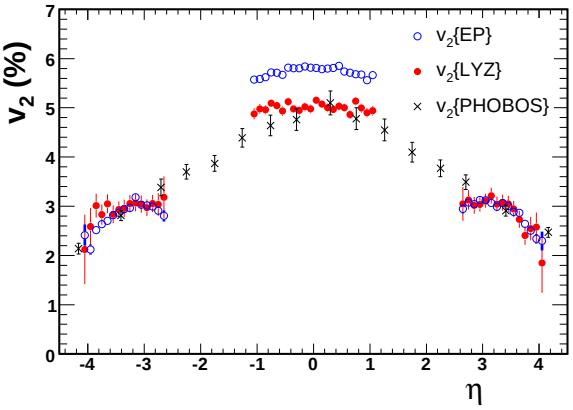

FIG. 3: (Color online) v_2 for charged hadrons from the Lee-Yang Zero Product Generating Function (solid circles) and from the Event-Plane method (open circles), as a function of pseudorapidity. Both sets of data have been averaged over p_T from 0.15 to 2.0 GeV/c and centrality from 10 to 40% of $\sqrt{s_{NN}}$= 200 GeV $Au+Au$ collisions. For comparison, the PHOBOS data (10–40%) [35] (crosses) are also shown. The error bars are shown only for the statistical uncertainties.

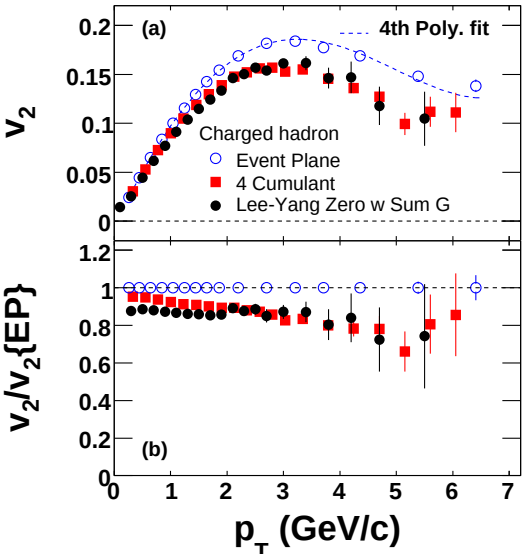

FIG. 4: (Color online) (a) v_2 as a function of p_T for charged hadrons with $|\eta| < 1.0$ in 10–40% $Au+Au$ collisions, at $\sqrt{s_{NN}}$= 200 GeV, from the Event-Plane method (open circles), 4-particle cumulant method (solid squares), and Lee-Yang Zero method (solid circles) with Sum Generating Function. (b) The ratios to the polynomial fit to $v_2\{\mathrm{EP}\}$ are shown for $v_2\{4\}/v_2\{\mathrm{EP}\}$ and $v_2\{\mathrm{LYZ}\}/v_2\{\mathrm{EP}\}$ as a function of transverse momentum. The error bars are shown only for the statistical uncertainties.

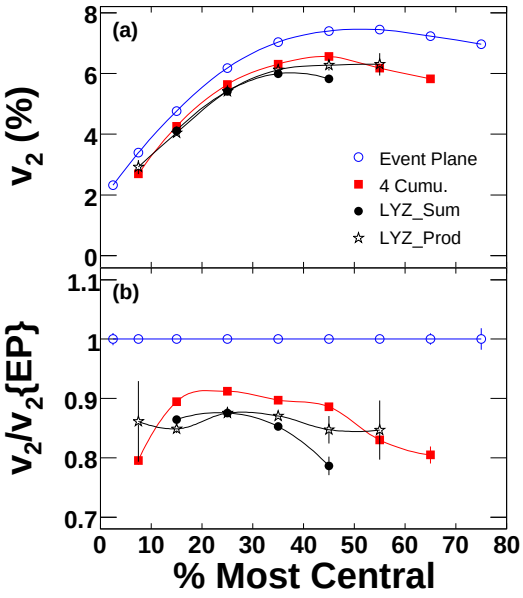

FIG. 5: (Color online) (a) p_T-integrated charged hadron v_2 in the TPC as a function of geometrical cross section. Shown are the Event-Plane method ($v_2\{EP\}$) (open circles), Lee-Yang Zero method with Sum Generating Function (solid circles), Lee-Yang Zero method with Product Generating Function (open stars), and 4-particle cumulant method ($v_2\{4\}$) (solid squares). For the TPC, $\mid \eta \mid < 1.0$ was used, except for Lee-Yang Zero method with Product Generating Function where the η limit went to 1.3. (b) v_2 divided by $v_2\{EP\}$. All data are from $\sqrt{s_{NN}} = 200$ GeV $Au + Au$ collisions. The error bars are shown only for the statistical uncertainties.

B. K^0_S and Λ

In order to estimate the particle dependence of systematic errors, K^0_S mesons and Λ baryons were analyzed with different flow analysis methods. Figure 6 shows 10–40% $v_2(p_T)$ of (a) $\Lambda + \overline{\Lambda}$ and (b) K^0_S obtained with the Event-Plane, Lee-Yang Zero, and η-subevent methods. Ratios of v_2 from these various methods to the Event-Plane method are shown in Fig. 6 (c) and (d) for $\Lambda + \overline{\Lambda}$ and K^0_S , respectively. The results from Lee-Yang Zero method are about 10% lower than those from the Event-Plane method. This is consistent with charged particles, indicating that non-flow effects for K^0_S and Λ are also reduced in the Lee-Yang Zero method. However, the ratio of the Lee-Yang Zero to Event-Plane method appears to be flat up to 5 GeV/c, considering the large statistical uncertainties. This is again similar to the trend observed for charged particle Lee-Yang Zero results, which are shown as shaded bands. The results for the η-subevent method are higher than for the Event-Plane method especially at low p_T. The $v_2\{\eta\}/v_2\{\mathrm{EP}\}$ ratio can be better understood by factorizing the ratio into an observed v_2 term and a resolution term $(v_2^{obs}\{\eta\}/v_2^{obs}\ \{\mathrm{EP}\})\times(resolution\{\mathrm{EP}\}/resolution\{\eta\})$. In this analysis we calculate the η subevent resolution by correlating the event planes from the different η hemispheres. In this case, the non-flow effects are reduced in both v_2^{obs} and the resolution. These factors contribute in the opposite direction to $v_2\{\eta\}/v_2\{\mathrm{EP}\}$; non-flow in the resolution term increases the ratio while non-flow in the v_2^{obs} term decreases the ratio. The $v_2\{\eta\}/v_2\{\mathrm{EP}\}$ ratio is greater than unity because the resolution is more sensitive to non-flow than v_2^{obs} and the decrease with p_T is caused by the increase of non-flow effects in $v_2^{obs}\{\mathrm{EP}\}$ with increasing p_T.

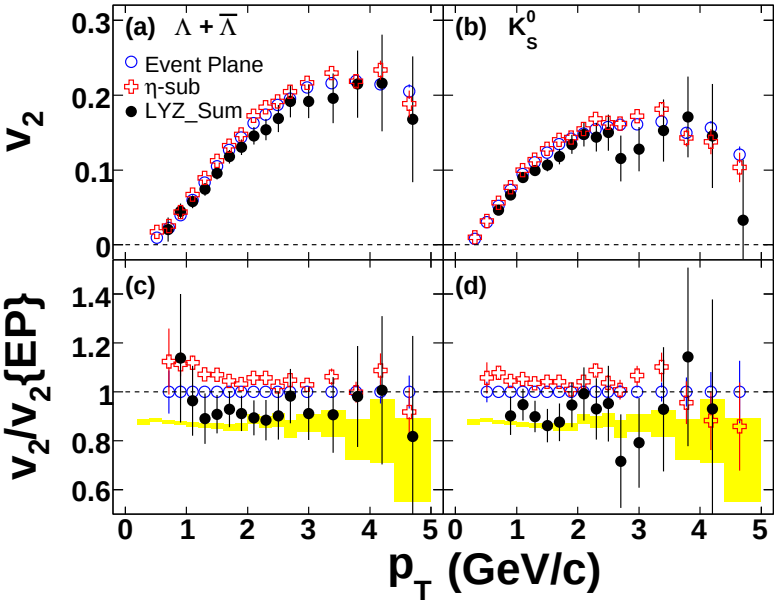

FIG. 6: (Color online) v_2 as a function of p_T for 10–40% centrality using Event-Plane method (open circles), Lee-Yang Zero method with Sum Generating Function (solid circles), and η-subevent method (open crosses), are shown in (a) and (b) for Λ and K^0_S, respectively. All data are from $\sqrt{s_{NN}}$= 200 GeV $Au+Au$ collisions. The ratios, $v_2\{\mathrm{LYZ}\}/v_2\{\mathrm{EP}\}$ and $v_2\{\eta\}/v_2\{\mathrm{EP}\}$, are shown in (c) and (d) for Λ and K^0_S, respectively. $v_2\{\mathrm{LYZ}\}/v_2\{\mathrm{EP}\}$ ratios for charged hadrons are shown as shaded bands. The error bars are shown only for the statistical uncertainties.

C. Systematic uncertainty of Λ from feed-down

We estimate the reaction plane orientation from the azimuthal distribution of charged particles measured with the TPC ($|\eta| < 1.3$), constructing the second harmonic event plane flow vector Q_2. The TPC is also used to reconstruct Λ and $\overline{\Lambda}$ hyperons via their charged decay daughters, $\pi^{\pm}$ or $p(\overline{p})$. Elliptic flow of Λ and $\overline{\Lambda}$ is measured by correlating the hyperon azimuthal angle with the event plane vector Q_2. Although the correlation strength is mainly defined by the hyperon elliptic flow, $v_2^{\Lambda,\overline{\Lambda}}$, in such an approach other sources of correlations (non-flow effects) may contribute

and bias the measured $v_2^{\Lambda,\overline{\Lambda}}$ values.

We do not distinguish between Λ and $\overline{\Lambda}$ particles produced from the secondary decays (for example, $\Xi^- \to \Lambda + \pi^-$ ($\overline{\Xi}^+ \to \overline{\Lambda} + \pi^+$), $\Sigma(1385)^- \to \Lambda + \pi^-$ ($\Sigma(1385)^+ \to \overline{\Lambda} + \pi^+$) or $\Sigma^0 \to \Lambda + \gamma$) and hyperons which originate directly from the primary interaction. Indirect hyperons lead to the presence of extra correlations that are not related to the reaction plane between hyperons and other charged particles produced in the collision. Note that the charge combinations for these correlations are opposite for Λ and $\overline{\Lambda}$ particles.

To estimate the contribution of these non-flow correlations from hyperon feed-down effects we use the charge subevent technique. For this method we introduce two event plane vectors: Q_2^+ constructed from positively charged particles and Q_2^- from negatively charged particles. We then estimate the contribution to the Λ and $\overline{\Lambda}$ elliptic flow measured with the full event plane vector Q_2 by considering the following ratio:

$$\delta R\{\text{FeedDown}\} = \frac{\mathrm{v}_2^{\Lambda}\{\mathrm{Q}_2^-\} + \mathrm{v}_2^{\overline{\Lambda}}\{\mathrm{Q}_2^+\}}{\mathrm{v}_2^{\Lambda}\{\mathrm{Q}_2^+\} + \mathrm{v}_2^{\overline{\Lambda}}\{\mathrm{Q}_2^-\}}. \tag{20}$$

Here $v_2^{\Lambda,\overline{\Lambda}}\{Q_2^{\pm}\}$ denotes Λ ($\overline{\Lambda}$) elliptic flow values measured from correlations with $Q_2^{\pm}$. The numerator in Eq. (20) contains the contributions from non-flow correlations attributed to feed-down effects, while the denominator is free of this. From this study we found that contribution of non-flow effects from feed-down of secondary Λ and $\overline{\Lambda}$ hyperons is $\leq 2\%$.

D. Other systematic uncertainties

In order to estimate the systematic uncertainties in the identified hadron v_2, we employed the standard Event-Plane method, the η-subevent method, and the Lee-Yang Zero method. The results of the analysis for Λ+$\overline{\Lambda}$ and K_S^0 are shown in Fig. 6. The ratios to the event plane results are shown in the lower panels. We limited ourselves to the 10–40% centrality bin where the results from the Lee-Yang Zero method are most reliable. For comparison, the charged hadron results from the $v_2\{\mathrm{LYZ}\}/v_2\{\mathrm{EP}\}$ ratios (Fig. 4) are also shown in the figure as shaded bands. There is no clear p_T dependence of the ratio $v_2\{\mathrm{LYZ}\}/v_2\{\mathrm{EP}\}$ for either Λ+$\overline{\Lambda}$ in (c) or for K_S^0 in (d) although, within the statistical errors, similar trends are seen for both identified particles. The overall systematic errors are on the order of 15% in the p_T region studied. The subevent method, however, introduced an additional factor described in Section II C 2 that leads to the enhanced ratio for both Λ+$\overline{\Lambda}$ and K_S^0. This opposite effect is also within the order of 15%.

In order to obtain good statistics, the Event-Plane method is used for most of analyses of identified particles. Depending on the analysis method, systematic uncertainties from variations in particle identification cuts, background subtractions, and summing of centrality bins are also estimated. By varying particle identification (PID) cuts, which change signal over background ratios by a factor of 3, the systematic uncertainty from the PID cuts is estimated to be about 5% below 4 GeV/c. From 4 GeV/c to 6 GeV/c, this effect is larger in central collisions than peripheral collisions, and in the 0–10% bin it is about a 10% effect. To estimate the uncertainty from background subtractions, background variations from different second and fourth order polynomial fit functions in Fig. 1 were propagated to measured v_2 values with Eq. 1. The effect is less than 3%. When combining centralities, the combined v_2 value should be a yield-weighted average of v_2 values in small centrality bins. In the method used previously [2], v_2 values are taken as weighted observed v_2 corrected by weighted event plane resolution. With the v_2 versus m_{inv} method, similar corrections were calculated. They are less than 5% below 6 GeV/c.

In summary, for charged particles, a 15% difference for $\langle v_2 \rangle$ at mid-rapidity for 10–40% collisions between the event plane and the Lee-Yang Zero methods has been observed. The difference between $v_2\{\mathrm{EP}\}$ and $v_2\{4\}$ is smaller, $\sim$10%, but for the more peripheral and more central collisions it seems to be closer to 20%. For $v_2(p_t)$ of K_S^0 and Λ, a difference also is observed between the Event-Plane and the Lee-Yang Zero methods. However, the comparison with charged particles shows that, within the much larger statistical uncertainties for the Λ and K_S^0 analysis, the different magnitudes of the estimated flow from the different methods observed are similar for charged particles and for the Λ and K_S^0 particles. The uncertainty used is 15%. In a latter section, the results are presented for Ξ^- and the Ω^-. For these particles, due to limited statistics, only the Event-Plane method has been used and therefore no real estimate of the systematic error is available. Instead what was done, was to show the estimated systematic uncertainties obtained for the charged particles, taking into account effects from background estimation, summing centralities, and variations in cuts. A summary of our best knowledge of systematic errors is given in Table I.

centrality	0–80%	40–80%	10–40%	0–10%
charged hadrons	20%	20%	15%	20%
identified particles	N/A	N/A	15%	N/A

TABLE I: Systematic errors of v_2 estimated from the different flow methods summarized as a function of centrality for $\sqrt{s_{NN}} =$ 200 GeV $Au+Au$ collisions for unidentified charged hadrons and identified particles. The p_T region covered for charged hadrons is $0.5 < p_T < 7.0$ GeV/c and for identified particles K^0_S, p, and Λ is $0.5 < p_T < 5.0$ GeV/c.

IV. DISCUSSION

A. Charged hadrons

Figure 5 shows that for the Lee-Yang Zero method the sum and product generating functions agree, but are slightly lower than the four-particle cummulant method. The Event-Plane method appears to be about 15% higher than the other methods. This could be due to either non-flow contributions increasing the event plane results or fluctuations of v_2 decreasing the multi-particle methods [8]. Charged hadron results give an indication of the systematic uncertainty inherent in the Event-Plane method, which is used for most of the identified particles in this paper in order to reduce statistical errors. The p_T dependence of this effect can be seen in Fig. 4. Note that the mentioned 15% non-flow effect is extracted only from the 10–40% centrality window. In other centrality bins, the effect may be larger. It should be possible to study this effect as a function of p_T for all centralities with a future higher statistics data sample.

B. Identified hadrons

The results for $\pi^+ + \pi^-$, $\overline{p} + p$, K^0_S, $\Lambda + \overline{\Lambda}$, $\Xi^- + \overline{\Xi}^+$ and $\Omega^- + \overline{\Omega}^+$ are shown in Figure 7 for various centralities of $Au + Au$ collisions at 200 GeV. Shown are results for minimum bias and three other centrality bins. All $v_2(p_T)$ results are from the Event-Plane method. The systematic uncertainties extracted from PID cuts, background subtractions, and combining centralities, are shown as shaded bars in the figure. The systematic uncertainty in the method itself is not included. The shaded band in plot (c) indicates the systematic uncertainties for K^0_S and Λ for the 10–40% centrality bin, as discussed in the previous section. In addition, the systematic uncertainties for pions and protons from Event-Plane and η-subevent analysis are plotted as the shaded band in plot (a). The results from an ideal hydrodynamic model [36, 37] are displayed by the lines.

Figure 7 shows that the ideal hydrodynamic model calculations reproduce the mass ordering of v_2 in the relatively low p_T region (the heavier the mass, the smaller the v_2) but overshoot the values of v_2 for all centrality bins. There seems to be a p_T dependence in the disagreement, and for more central collisions, the overshoot does not take place until a higher p_T. In other words, the system agrees better with the ideal hydrodynamic model for more central collisions. Although we do not expect a large non-flow contribution at the low transverse momentum region, the centrality selections between the model calculations based on the impact parameter and the data based on the multiplicity are different, which may also affect the model and data agreement. Note that we observe possible negative values of $v_2(p_T)$ for the heavier hadrons at the lowest observed p_T in the most central $Au + Au$ collisions.

At higher p_T, the hydrodynamic type mass ordering evolves into a hadron type ordering (baryons versus mesons). There the results show two groups depending on the number of quarks in the hadron; the baryons are higher than the mesons. The effects are clearly shown in plots (a), (b) and (c). In the most central bin (d), however, the effect is less pronounced. For all p_T, v_2 evolves toward larger values in going from central collisions to more peripheral collisions. The ideal hydrodynamic model also predicts this centrality dependence though it fails to describe the behavior at higher p_T.

Figure 8 shows the same results as in Fig. 7 but as a function of the transverse kinetic energy $K_T = m_T - m = \sqrt{p_T^2 + m^2} - m$. Here m is the particle mass. In this case, v_2 for all hadrons at low K_T follow a universal curve, which appears to be monotonically increasing and almost linear in all centrality bins. The observed increase is slowest for the most central 0–10% bin. The corresponding results from the ideal hydrodynamic model calculations are also shown in the figure. The mass ordering in the model calculation is reversed when one plots v_2 versus $m_T - m$: the higher the mass the larger the value of v_2. While the data seem to show a scaling in the low $m_T - m$ region, the model results do not show any scaling.

In Figs. 9, 10, and 11 we discuss the properties of the centrality dependence of the observed scaling including both the low $p_T \leq 2$ GeV/c and the intermediate $2 \leq p_T \leq 5$ GeV/c regions. Figure 9 shows v_2 scaled by the number of constituent quarks, v_2/n_q, for all strange hadrons including the pure multi-strange hadrons ϕ and Ω. The left panels show the results as a function of p_T scaled by the number of quarks, p_T/n_q, and the right panels as a function of

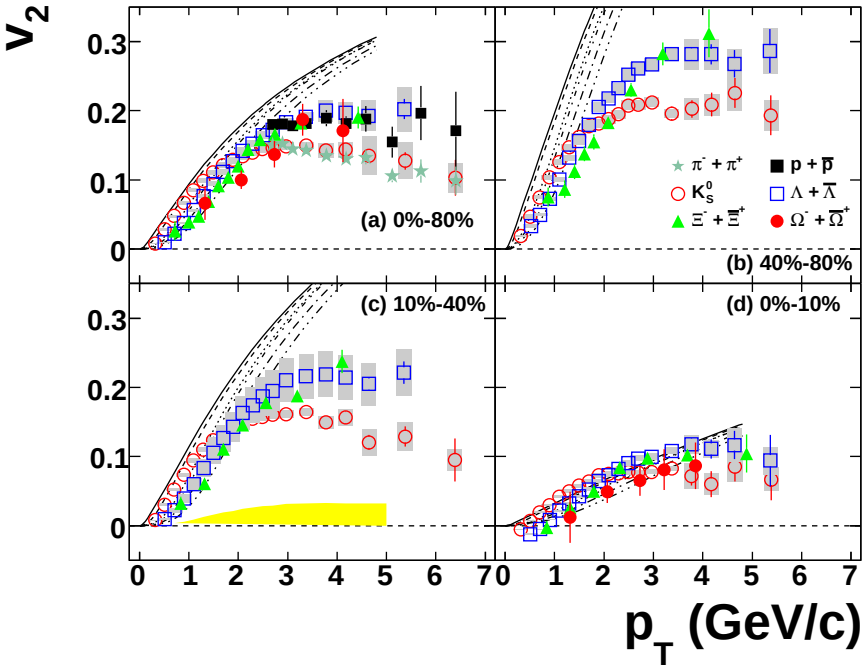

FIG. 7: (Color online) v_2 of K^0_S (open circles), Λ (open squares), Ξ (filled triangles) and Ω (filled circles) as a function of p_T for (a) 0–80%, (b) 40–80%, (c) 10–40% and (d) 0–10% in $Au+Au$ collisions at $\sqrt{s_{NN}}$= 200 GeV. The error bars represent statistical uncertainties. The bands on the data points represent systematic uncertainties as discussed in the text. For comparison, pion (stars) and proton (filled squares) results are shown in (a). The systematic uncertainty of non-flow for K^0_S and Λ for 10–40% (c) is plotted as a shaded band near 0. For comparison, results from ideal hydrodynamic calculations [36, 37] are shown: at a given p_T, from top to bottom, the lines represent the results for π, K, p, Λ, Ξ, and Ω.

K_T/n_q. Plots (a) and (b) are the corresponding scaled results. It appears that the scaling works better when the data are plotted as a function of transverse kinetic energy K_T, as in plot (b). The ideal hydrodynamic results are also shown in both presentations. Clearly, the hydrodynamic distributions are also better scaled when plotted versus K_T. Polynomial fits were made for all hadrons. The results are shown as dot-dot-dashed lines in plot (a) and (b). The ratios of the data and the hydrodynamic lines over the polynomial fit are shown in plots (c) and (d). For all data, there is scaling at $p_T/n_q \geq 0.7$ GeV/c or $K_T/n_q \geq 0.2$ GeV/c^2. The errors from the multi-strange hadrons ϕ [16] and Ω are large, see plots (e) and (f), but are consistent with the scaling. This observed n_q-scaling provides strong evidence that these hadrons are formed via a coalescence process at the end of the partonic evolution [11, 13]. Comparing to the light non-strange hadrons, strange hadrons participate much less in later stage hadronic rescattering processes [38]; thus, these distributions directly reflect the early dynamics of the collision at RHIC. It is interesting to note that the ideal hydrodynamic results scale neither at low p_T nor intermediate p_T. Therefore the observed scaling *cannot* be a general characteristics of hydrodynamic model calculations [17], although such calculations do show the observed mass ordering in the low p_T region.

Figures 10 and 11 show the centrality dependence of the scaling properties and the ratios, respectively. Similar to the observations from Fig. 9, the conclusions from Figs. 10 and 11 are:

1. There is a clear number-of-quark scaling at intermediate p_T and better scaling in K_T for all hadrons studied here, but no scaling is observed at low p_T.

2. The ideal hydrodynamic model results do not show any scaling over the region $0.2 \leq p_T \leq 5$ GeV/c.

3. These results are true for all centrality bins.

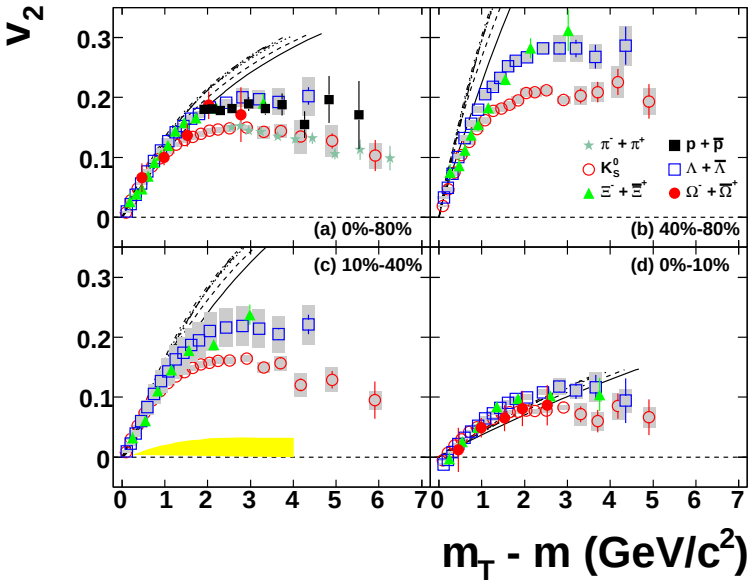

FIG. 8: (Color online) v_2 in Fig. 7 is re-plotted as a function of $m_T - m$ for K^0_S (open circles), Λ (open squares), Ξ (filled triangles) and Ω (filled circles), for (a) 0–80%, (b) 40–80%, (c) 10–40% and (d) 0–10% in $Au + Au$ collisions at $\sqrt{s_{NN}}$= 200 GeV. For comparison, pion (stars) and proton (filled squares) results are shown in (a). The ideal hydrodynamic calculations in Fig. 7 are also shown as a function of $m_T - m$.

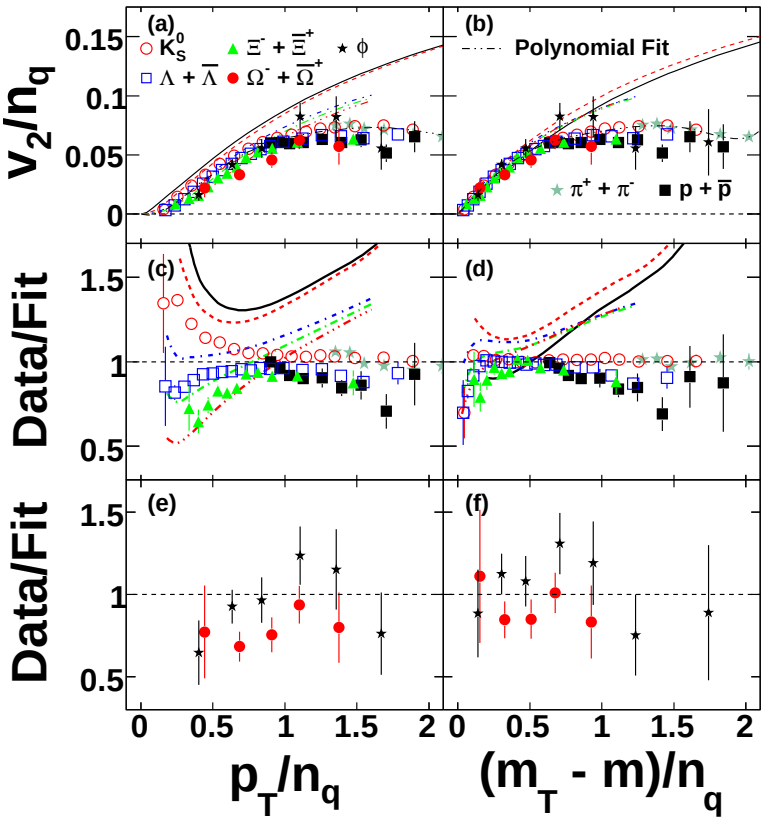

FIG. 9: (Color online) Number-of-quark scaled v_2 (v_2/n_q) of identified particles versus p_T/n_q in (GeV/c) (left column) and $(m_T - m)/n_q$ in (GeV/c^2) (right column). Dot-dot-dashed lines are the results of 6th order polynomial fits to K^0_S, Λ, Ξ, and Ω. The ratios of the data points over the fit are shown in panels (c) and (d) for K^0_S, π, p, Λ, and Ξ, and in panels (e) and (f) for Ω and ϕ [16]. The error bars are shown only for the statistical uncertainties. Ideal hydrodynamic calculations for π, K, Λ, Ξ, and Ω are presented by solid lines, dashed lines, dot-dashed lines, dot-long-dashed lines, and dot-dot-dot-dashed lines, respectively. The ratio of hydrodynamic calculations over the fit are also shown for comparison in panels (c) and (d). The data are from minimum bias (0–80%) $Au + Au$ collisions at $\sqrt{s_{NN}} = 200$ GeV.

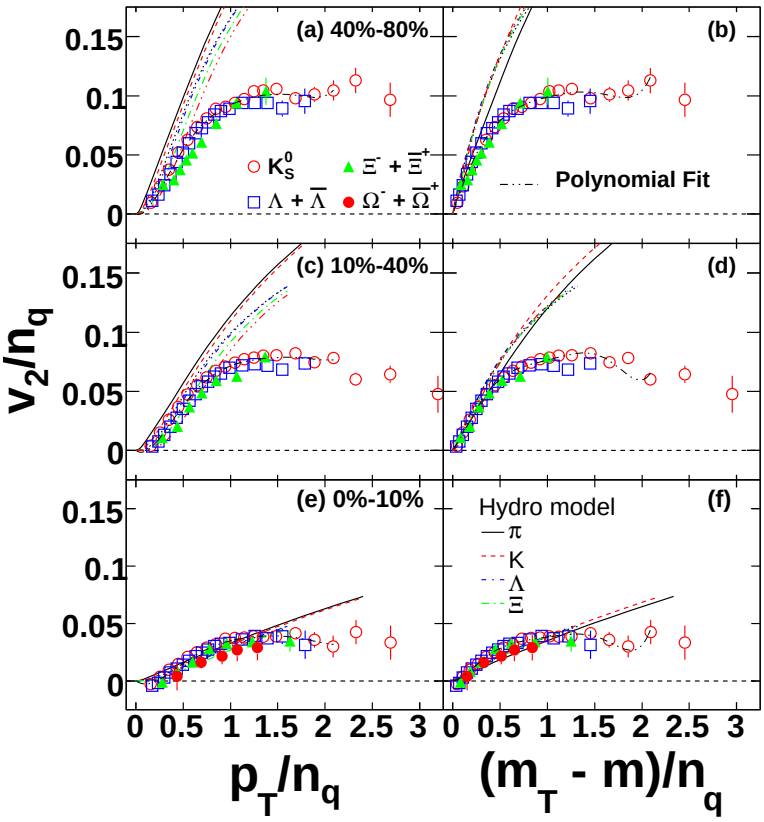

FIG. 10: (Color online) Centrality dependence of the number-of-quark scaled v_2 (v_2/n_q) of identified particles versus p_T/n_q in (GeV/c) (left column) and $(m_T - m)/n_q$ in (GeV/c^2) (right column). The error bars are shown only for the statistical uncertainties. The 6th order polynomial fits are shown as dot-dot-dashed-lines. Ideal hydrodynamic curves [37] are also plotted. All data are from $\sqrt{s_{NN}}$= 200 GeV $Au + Au$ collisions.

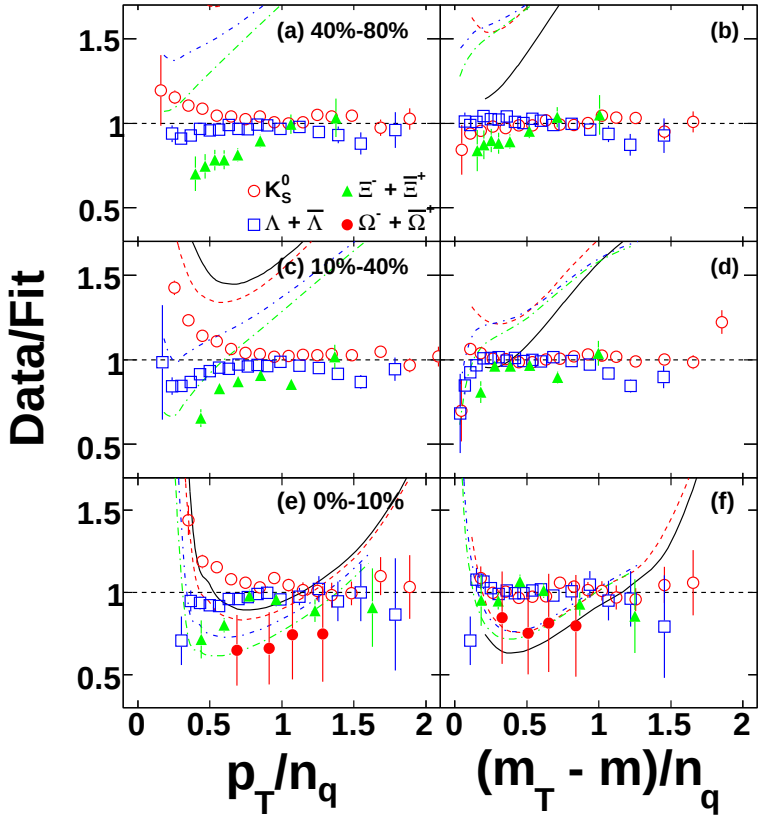

FIG. 11: (Color online) Centrality dependence of the v_2/n_q ratio to a common polynomial fit is shown versus p_T/n_q in (GeV/c) (left column) and $(m_T - m)/n_q$ in (GeV/c^2) (right column). The error bars are shown only for the statistical uncertainties. Ideal hydrodynamic calculations over the same fit are also shown for comparison. Ideal hydrodynamic calculations for π, K, Λ, Ξ and Ω are presented by solid lines, dashed lines, dot-dashed lines, dot-long-dashed lines, and dot-dot-dot-dashed lines, respectively. All data are from $\sqrt{s_{NN}}$= 200 GeV $Au + Au$ collisions.

	$\sigma_{trig}/\sigma_{geom}$	0–80%	40–80%	10–40%	0–10%
62.4 GeV	ε_{part}	0.3919±0.0003	0.5426±0.0004	0.2927±0.0003	0.1108 ±0.0002
	N_{part}	122±3	39±5	167±7	320±3
	N_{bin}	249±13	50±10	338±18	797±9
200 GeV	ε_{part}	0.3843±0.0001	0.5343±0.0002	0.2829±0.0001	0.1054±0.0001
	N_{part}	126±8	42±7	173±10	326 ± 6
	N_{bin}	293±36	57 ± 14	393± 47	939 ± 72

TABLE II: List of participant eccentricity ε_{part}, number of participants N_{part}, and number of binary collisions N_{bin}, from a Glauber calculation [39, 40] for minimum bias and three other centrality bins. The errors are statistical from the calculations only. The biggest systematic error is probably from the centrality binning based on the impact parameter compared to the binning of the data based on the multiplicity. All parameters for 62.4 GeV Au+Au collisions are calculated in a similar fashion as for 200 GeV collisions. The p+p cross sections used were 36 mb at 62.4 GeV and 42 mb at 200 GeV.

C. Universal scaling?

In order to analyze the centrality dependence of the scaling properties, we normalize the n_q-scaled elliptic flow v_2 by the participant eccentricity ε_{part} from a Monte Carlo Glauber calculation [39, 40]. (See Table II for ε_{part}.) The results are depicted in Fig. 12. The plots (a) and (b) show the doubly scaled quantities from three centrality bins as a function of p_T/n_q and $(m_T - m)/n_q$, respectively. Both plots show an initial rise and a turn over to a flat region in the higher p_T region. It is interesting to see in (a) and (b) that at a given centrality, the elliptic flow of all hadrons are scaled as observed in the minimum bias case (Fig. 9). After the geometric effect has been removed by dividing by ε_{part} in (a) and (b), the build up of stronger collective motion in more central collisions becomes obvious in the measured elliptic flow. This is consistent with the ideal hydrodynamic model calculations, shown as lines in (b), although the model results are much closer together. However, clearly there is no scaling amongst different collision centralities. Neither our data nor the model results indicate universal scaling with eccentricity. A careful inspection of the results presented in Ref. [41] shows there is no disagreement between data; rather, the statement of the universal scaling in Ref. [41] is not supported by the data.

To further clarify the issue, instead of dividing the measured v_2 by the corresponding eccentricity ε_{part}, we plot $v_2(m_T - m)/(n_q \times \langle v_2 \rangle)$ for K^0_S , Λ , and Ξ in Fig. 12 (c). The values of $\langle v_2 \rangle$ (see Table III) are obtained by averaging v_2 as a function of transverse momentum weighted with the measured spectra. As one can see in the figure, for a given hadron, this scaling seems to work better. However, different hadrons seem to have different values of v_2, especially for the top 10% centrality bin at the higher m_T.

Figure 12 (d) shows the doubly scaled v_2 again. But this time, the integrated values of v_2 are extracted from the measurements of unidentified charged hadrons $\langle v_2 \rangle_{ch}$ at the corresponding centrality bins. In this case, it appears that the scaling works better. It is interesting to point out that at the most central bin, see inset in Fig. 12 (d), the values of v_2 become negative at low p_T for all hadrons. This is most likely caused by the strong radial flow developed in central Au+Au collisions [42]. Similar behavior has also been observed in v_2 of Λ at SPS [43].

D. Integrated v_2/ϵ_{part} versus collision centrality

$\sigma_{trig}/\sigma_{geom}$	40–80%	10–40%	0–10%
$h^{\pm}$	0.0735 ± 0.000163	0.0576 ± 0.000064	0.0283 ± 0.000112
K^0_S	0.0707 ± 0.0008 ± 0.0013	0.0513 ± 0.0005 ± 0.0013	0.0212 ± 0.0011 ± 0.0012
ϕ	0.0851 ± 0.0111 ± 0.0020	0.0658 ± 0.0082 ± 0.0016	0.0210 ± 0.0116 ± 0.0050 (0–5%)
Λ	0.0899 ± 0.0010 ± 0.0013	0.0609 ± 0.0006 ± 0.0019	0.0221 ± 0.0012 ± 0.0029
Ξ	0.0858 ± 0.0045 ± 0.0000	0.0577 ± 0.0032 ± 0.0023	0.0220 ± 0.0028 ± 0.0015

TABLE III: The p_T-averaged v_2 of identified particles (particle + anti-particle) from three centrality bins in $\sqrt{s_{NN}}$= 200 GeV Au+Au collisions. The Event-Plane method was used to extract the values of v_2. Statistical and systematic errors are shown as the first and second errors, respectively.

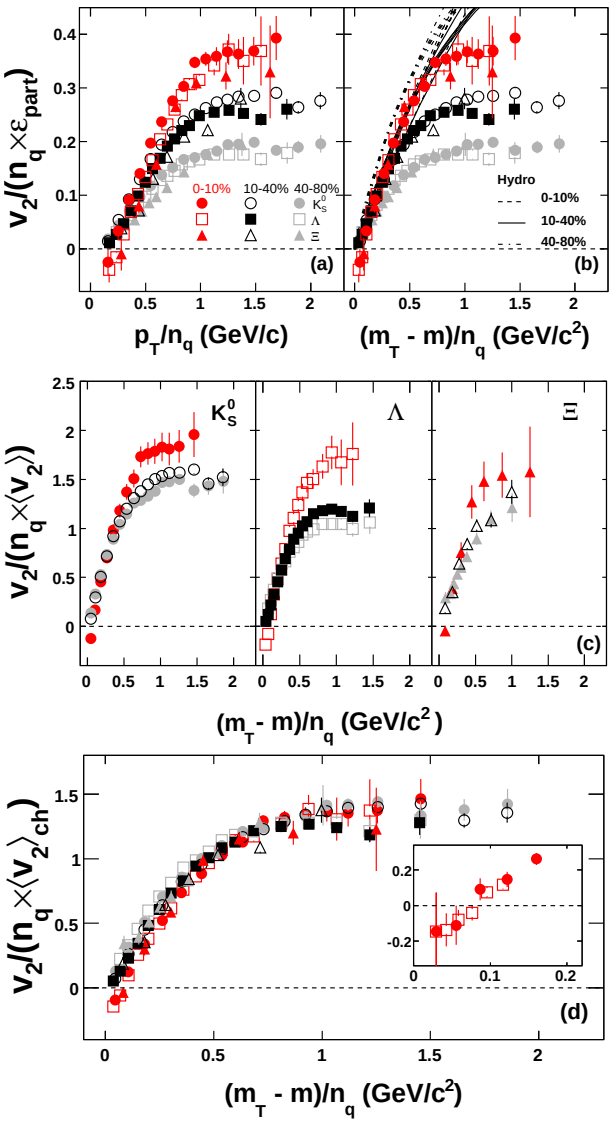

FIG. 12: (Color online) v_2 scaled by the number of quarks (n_q) and participant eccentricity (ε_{part}), (v_2/ ($n_q \times \varepsilon_{part}$)), of identified particles (particle + anti-particle) versus (a) the scaled p_T/n_q and (b) $(m_T - m)/n_q$ for three centrality bins. For comparison, ideal hydrodynamic model calculations [37] are shown as lines in (b). In (c) is shown the data from (b) scaled by the integrated v_2 of each particle, instead of ε_{part}. In (d) is shown the data from (b) scaled by the integrated v_2 of all charged hadrons. The insert in (d) expands the low m_T region. The error bars are shown only for the statistical uncertainties. All data are from $\sqrt{s_{NN}}$= 200 GeV $Au + Au$ collisions.

The integrated elliptic flow values in Table III were obtained from the measured $v_2(p_T)$ and separately parameterized p_T spectra. The $v_2(p_T)$ were integrated over p_T weighted with the yield distribution from functions fitted to the spectra. To extend v_2 to low p_T, a sixth order polynomial and a n_q-inspired function [44] were used to fit v_2. The v_2 values in the table are the average values from these two sets of parameterizations. The systematic uncertainties are taken as half of the differences between values from two sets of fits. The statistical errors as a function of p_T are fitted with third order polynomials and folded with the yield distributions into the errors of the integrated v_2. The spectra for K^0_S and Λ are from Ref. [45] and the spectra for Ξ are from Ref. [14]. Data for ϕ-mesons are from Ref. [16].

The centrality dependence of the ratio of the integrated elliptic flow (Table III) over the eccentricity (v_2/ε_{part}) for charged hadrons, K^0_S , ϕ-meson [16], Λ and Ξ are shown in Fig. 13. All these results are from the Event-Plane method and the number of participants is the average in the centrality bin. For comparison, results from an ideal hydrodynamic calculation [37, 46] are also shown as dashed lines. This ratio, to some extent reflects the strength of the collective expansion. At more central collision, one would expect a stronger expansion, hence the larger value of the ratio. This is what one sees in Fig. 13 for charged hadrons. For identified hadrons, the increasing trend as a function

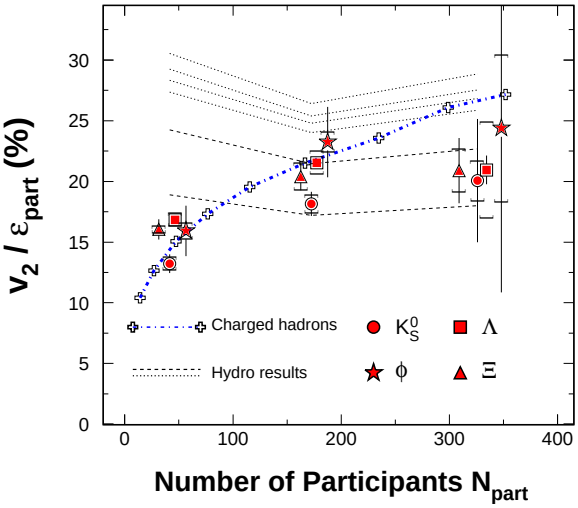

FIG. 13: (Color online) Centrality dependence of v_2/ε_{part} versus number of participants for charged hadrons (crosses), K^0_S (circles), ϕ (stars) [16], $\Lambda + \overline{\Lambda}$ (squares) and $\Xi + \overline{\Xi}^+$ (triangles). Both unidentified charged hadron and identified hadron v_2 were analyzed with the standard Event-Plane method. All data are from $\sqrt{s_{NN}}$= 200 GeV $Au+Au$ collisions. The data points are displaced slightly horizontally for clarity. The statistical uncertainties and the systematic uncertainties are shown as bars and brackets, respectively. Ideal hydrodynamic model calculations are also shown as dashed lines [37, 46] for, from top to bottom, Ω, Ξ, Λ, p, K, and π.

of N_{part} is there despite the large error bars. In the ideal hydrodynamic calculations [37, 46], the first order phase transition and freeze-out temperatures are set to be 165 MeV and 130 MeV, respectively. With these parameters, the ideal hydrodynamical model results describe the pion, kaon and proton transverse momentum spectra [37, 46]. In a pure hydrodynamic model, one deals with energy-momentum cells rather than any specific type of hadrons, thus the initial condition, the equation of state and the freeze-out conditions used in the calculation are the same for all hadrons. Such assumptions may not be applicable to all hadrons since some of them will continue to interact even after hydrodynamic freeze-out [47].

As expected in an equilibrium scenario, the model results show little sensitivity to the collision centrality. However, it is interesting to note that there is a clear hadron mass dependence of v_2 normalized by ε_{part} from the model calculations which is not seen in the data. It is not clear whether the mass dependence is from the collective motion at early time or is the effect of the hadronization process in the calculation. On the data side, the errors are too large to allow comparisons with model results. As one can see in Fig. 13, after $N_{part} \sim 170$, the measured ratios for the strange particles approach that from the ideal hydrodynamic model calculations. The consistency between model results and data indicates that the system created in 200 GeV $Au + Au$ collisions may reach local thermalization in central collisions when the number of participants is larger than ~ 170.

E. Energy dependence

The transverse momentum dependence of eccentricity-scaled v_2 ratios are shown in Fig. 14. Plots (a) and (b) show the ratio of data from 62.4 GeV ($Au + Au$ collisions) and 17.2 GeV ($Pb + Pb$ collisions [43]) over 200 GeV $Au + Au$ collision data, respectively. It has been observed [48] that since the charged multiplicity production per participant is proportional to the square root of the CM energy [48], $dN/d\eta/\langle N_{part}/2\rangle \propto \sqrt{s_{NN}}$, a stronger flow is expected from higher energy collisions [49]. In Fig. 14, the ratios for both K^0_S and Λ are similar. While the higher energy ratios show a decreasing trend as a function p_T, the lower energy ratios seem to increase with transverse momentum. In the low p_T region ($\leq$ 1.5 GeV/c), the strength of flow is similar in 200 GeV and 62.4 GeV $Au + Au$ collisions. For the 0–80% Au+Au collisions, the values of the participant eccentricity from 62.4 and 200 GeV are 0.392 and 0.384, respectively. The lack of energy dependence in v_2 for K^0_S and Λ is due to the similarity in the participant eccentricity. The PHOBOS experiment reported a similar observation for the v_2 of charged hadrons [50]. As discussed in [48], from 62 GeV to 200 GeV, the participant-normalized charged hadron density at mid-rapidity increased by about 50%. However, we do not observe a change of a similar size in the participant eccentricity and v_2, indicating that a large

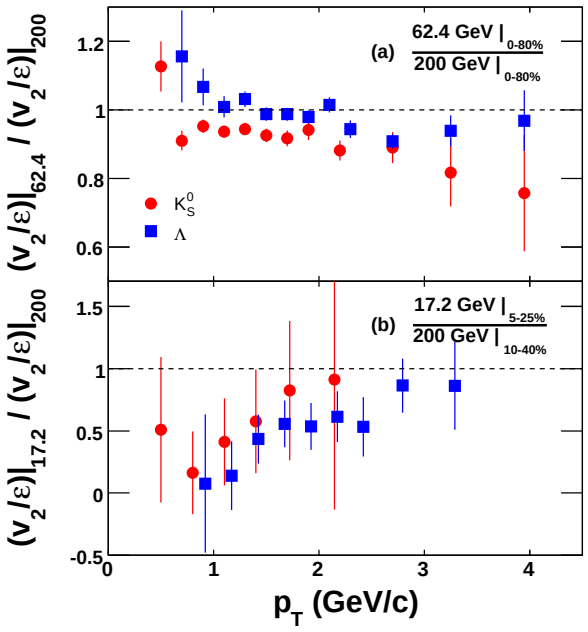

FIG. 14: (Color online) The p_T dependence of the eccentricity-scaled v_2 ratios of (a) 62.4 GeV and (b) 17.2 GeV [43] over 200 GeV data for K^0_S (circles) and $\Lambda + \overline{\Lambda}$ (squares). As indicated in (b), the SPS data points are from 5–25% and the RHIC data points are from 10–40%. Error bars are statistical only.

fraction of the particle production occurs at the later stage of heavy ion collisions at these beam energies.

The ratio is less than unity in the low p_T region (see Fig. 14 (b)) indicating that the flow is weaker in the lower energy $Pb+Pb$ collisions [43]. The collective velocity parameters, extracted from the transverse momentum spectra, are also found to be larger in 200 GeV $Au+Au$ collisions than those from 17.2 GeV $Pb+Pb$ collisions [11]. Since elliptic flow develops at a relatively early stage of the collisions, the observed increase in collective flow in $Au+Au$ collisions at RHIC is therefore caused by early partonic interactions [7, 8, 9].

Figure 15 shows the centrality dependence of v_2 normalized by the number of quarks and eccentricity $(v_2/(n_q\varepsilon_{part}))$ for identified hadrons from (a) 62.4 GeV [51] and (b) 200 GeV $Au+Au$ collisions. Within error bars, data from both energies are similar. At the low transverse energy region, the scaled v_2 shows almost a linear increase and then becomes flat. For more central collisions the turning point is at higher values of $(m_T-m)/n_q$. Recently, PHENIX has reported a charged hadron scaling with eccentricity, system size, and the transverse energy (m_T-m) up to 1 GeV/c^2 [41]. As one can see from the figure, at a given centrality, independent of the collision energy, there is a clear scaling: all values of $v_2/(n_q\varepsilon_{part})$ coalesce into a single distribution. On the other hand, it is clear in the figure that at different centralities the shape of the distributions are different, meaning that there is no scaling in the measured v_2 with the eccentricity, especially in the higher transverse energy region.

V. SUMMARY

We present STAR results on the elliptic flow v_2 of unidentified charged hadrons, strange and multi-strange hadrons from $\sqrt{s_{NN}} = 200$ GeV $Au+Au$ collisions at RHIC. The centrality dependence of v_2 over a broad transverse momentum range is presented. Comparison of different analysis methods are made in order to estimate systematic uncertainties. The rapidity dependence of the charged hadron v_2 from these measurements is consistent, at both mid-pseudorapidity and forward rapidities, with both STAR [8] and PHOBOS [35] reported results. In particular, the results for v_2 from the Lee-Yang Zero method for charged hadrons, K^0_S , and Λ are shown for the first time at RHIC. The non-flow effects, studied in the 10–40% centrality window, are on the order of 10% within $0.2 \le p_T \le 3$ GeV/c and up to 25% at $p_T \sim 6$ GeV/c.

In the relatively low p_T region, $p_T \le 2$ GeV/c, a scaling with $m_T - m$ is observed for identified hadrons under

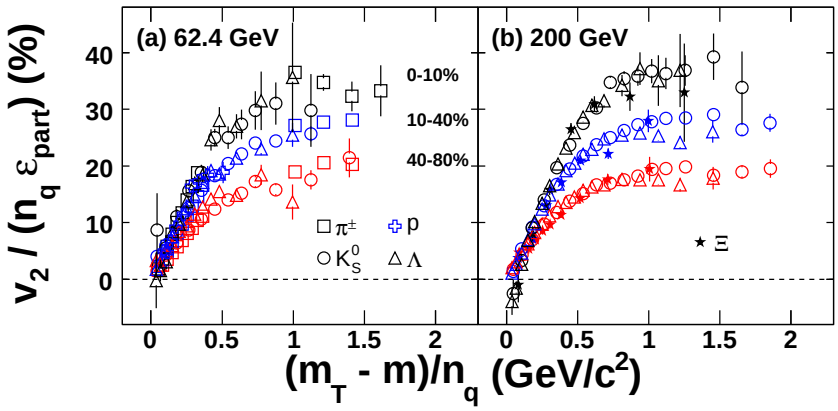

FIG. 15: (Color online) Centrality dependence of $v_2/(n_q\varepsilon_{part})$ for identified hadrons (particle + anti-particle) from (a) 62.4 GeV [51] and (b) 200 GeV $Au + Au$ collisions. Error bars are statistical only. For the 10–40% centrality the systematic uncertainty should be the same as in Fig. 7.

study in each centrality bin and there is a clear centrality dependence in the scaling. However, we do not observe $v_2(m_T - m)$ scaled by the participant eccentricity to be independent of centrality. The largest values of the participant eccentricity scaled v_2 are in the most central collisions. For the most central collisions (0–10%), negative values of v_2 at the lowest p_T studied have been observed for both K^0_S and Λ . This is the first time a negative v_2 in $Au + Au$ collisions at RHIC has been found. It is consistent with the strong expansion observed in hadron spectra analysis [11]. In the higher p_T region, $2 \leq p_T \leq 6$ GeV/c, number-of-quark scaling is observed for all particles under study. For the multi-strange hadron Ω, which does not suffer appreciable hadronic interactions, the values of v_2 are consistent with both $m_T - m$ scaling at low p_T and number-of-quark scaling at intermediate p_T.

As a function of collision centrality, an increase of p_T-integrated v_2 scaled by the participant eccentricity has been observed, indicating stronger collective flow in more central $Au + Au$ collisions. However, in the higher transverse energy region there is no scaling of v_2 with eccentricity.

The energy dependence of v_2 for K^0_S and Λ was presented for $\sqrt{s_{NN}} = 17$ GeV $Pb + Pb$, and 62 and 200 GeV $Au + Au$ collisions. No clear systematic trend was observed, but the differences were only on the order of 10%.

For comparison, results from ideal hydrodynamical model calculations were used. The calculations over-predict the data at $p_T \geq 2$ GeV/c. At low p_T , although the model predicts correctly the mass hierarchy observed in the data, there is no scaling with $m_T - m$, and no scaling with the number of quarks is observed throughout the p_T region for all hadrons. We observe that the mass ordering at low p_T alone is not sufficient to claim thermalization in $Au + Au$ collisions at RHIC.

VI. ACKNOWLEDGMENTS

We thank Jean-Yves Ollitrault and Nicolas Borghini for help in understanding the Lee-Yang Zero method.

We thank the RHIC Operations Group and RCF at BNL, and the NERSC Center at LBNL and the resources provided by the Open Science Grid consortium for their support. This work was supported in part by the Offices of NP and HEP within the U.S. DOE Office of Science, the U.S. NSF, the Sloan Foundation, the BMBF of Germany, CNRS/IN2P3, RA, RPL, and EMN of France, EPSRC of the United Kingdom, FAPESP of Brazil, the Russian Ministry of Sci. and Tech., the NNSFC, CAS, MoST and MoE of China, IRP and GA of the Czech Republic, FOM of the Netherlands, DAE, DST, and CSIR of the Government of India, Swiss NSF, the Polish State Committee for Scientific Research, Slovak Research and Development Agency, and the Korea Sci. and Eng. Foundation.

[1] S. Voloshin and Y. Zhang, Z. Phys. **C70**, 665 (1996).
[2] A.M. Poskanzer and S.A. Voloshin, Phys. Rev. C **58**, 1671 (1998).
[3] N. Borghini and J-Y. Ollitrault, Phys. Rev. C **70**, 064905 (2004).
[4] H. Sorge, Phys. Lett. **B402**, 251 (1997) and H. Sorge, Phys. Rev. Lett. **82**, 2048 (1999).
[5] J.-Y. Ollitrault, Phys. Rev. D **46**, 229 (1992).
[6] D. Teaney, J. Lauret, and E. Shuryak, Phys. Rev. Lett. **86**, 4783 (2001).
[7] C. Adler *et al.* (STAR Collaboration), Phys. Rev. Lett. **87**, 182301 (2001).
[8] J. Adams *et al.* (STAR Collaboration), Phys. Rev. C **72**, 014904 (2005).
[9] K.H. Ackermann, *et al.* (STAR Collaboration), Phys. Rev. Lett. **86**, 402 (2001).
[10] J. Adams *et al.* (STAR Collaboration), Phys. Rev. Lett. **92**, 052302 (2004).
[11] J. Adams *et al.* (STAR Collaboration), Nucl. Phys. **A757**, 102 (2005).
[12] J. Adams *et al.* (STAR Collaboration), Phys. Rev. Lett. **95**, 122301 (2005).
[13] D. Molnar and S.A. Voloshin, Phys. Rev. Lett. **91**, 092301 (2003).
[14] J. Adams *et al.* (STAR Collaboration), Phys. Rev. Lett. **98**, 062301 (2007).
[15] S. Afanasiev *et al.* (PHENIX Collaboration), Phys. Rev. Lett. **99**, 052301 (2007).
[16] B.I. Abelev *et al.* (STAR Collaboration), Phys. Rev. Lett. **99**, 112301 (2007).
[17] L.A. Linden Levy, J.L. Nagle, C. Rosen, and P. Steinberg, nucl-th/0709.3105.
[18] P.F. Kolb, U. Heinz, 'Quark Gluon Plasma 3'. Editors: R.C. Hwa and X.N. Wang, World Scientific, Singapore, p. 634; nucl-th/0305084.
[19] K. Adcox *et al.* (PHENIX Collaboration), Nucl. Phys. **A757**, 184 (2005).
[20] M. Gyulassy and L. McLerran, Nucl. Phys. **A750**, 30 (2005).
[21] S.A. Voloshin (STAR Collaboration), *Quark Matter 2006*, J. Phys. G **34**, S883 (2007).
[22] C. Adler *et al.* (STAR Collaboration), Phys. Rev. C **66**, 034904 (2002).
[23] H. Heiselberg and A. M. Levy, Phys. Rev. C **59**, 2716 (1999).
[24] R.S. Bhalerao, N. Borghini, and J.-Y. Ollitrault, Phys. Lett. **B580**, 157 (2004).
[25] R.S. Bhalerao, N. Borghini, and J.-Y. Ollitrault, Nucl. Phys. **A727**, 373 (2003); N. Borghini, R.S. Bhalerao, and J.-Y. Ollitrault, J. Phys. G **30**, S1213 (2004).
[26] N. Borghini, P.M. Dinh, and J.-Y. Ollitrault, Phys. Rev. C **64**, 054901 (2001).
[27] K. H. Ackermann *et al.* (STAR Collaboration), Nucl. Instrum. Methods A **499**, 624 (2003).
[28] C. Adler *et al.*, Nucl. Instrum. Methods A **470**, 488 (2001).
[29] C. Adler *et al.* (STAR Collaboration), Phys. Rev. Lett. **89**, 132301 (2002).
[30] J. Adams *et al.* (STAR Collaboration), Phys. Rev. Lett. **92**, 182301 (2004).
[31] N. Borghini, J.-Y. Ollitrault, Phys. Rev. C **70**, 064905 (2004).
[32] N. Bastid *et al.* (FOPI Collaboration), Phys. Rev. C **72**, 011901 (2005).
[33] X. Zhu, M. Bleicher, and H. Stöcker, J. Phys. G **32**, 2181 (2006).
[34] S.J. Sanders (BRAHMS Collaboration), J. Phys. G **34**, S1083 (2007).
[35] B.B. Back *et al.* (PHOBOS Collaboration), Phys. Rev. Lett. **94**, 122303 (2005).
[36] P. Huovinen, private communication, 2003.
[37] P. Huovinen and P.V. Ruuskanen, Ann. Rev. Nucl. Part. Sci. **56**, 163 (2006).
[38] H. van Hecke, H. Sorge, and N. Xu, Phys. Rev. Lett. **81**, 5764 (1998); Y. Cheng, F. Liu, Z. Liu, K. Schweda, and N. Xu, Phys. Rev. C **68**, 034910 (2003).
[39] M. Miller and R. Snellings, nucl-ex/0312008.
[40] M.L. Miller, K. Reygers, S.J. Sanders, P. Steinberg, Ann. Rev. Nucl. Part. Sci. **57**, 205 (2007).
[41] A. Adare *et al.* (PHENIX Collaboration), Phys. Rev. Lett. **98**, 162301 (2007); A. Taranenko, J. Phys. G **34**, S1069 (2007).
[42] P. Huovinen, P. Kolb, U. Heinz, P.V. Ruuskanen, and S.A. Voloshin, Phys. Lett. **B503**, 58 (2001).
[43] C. Alt *et al.* (NA49 Collaboration), Phys. Rev. C **75**, 044901 (2007).
[44] X. Dong, S. Esumi, P. Sorensen, N. Xu, and Z. Xu, Phys. Lett. **B597**, 328 (2004).
[45] J. Adams *et al.* (STAR Collaboration), nucl-ex/0601042.
[46] P. Huovinen, private communication 2006. $T_c = 165$ MeV, $T_f = 130$ Mev, EoS = Q, first order phase transition.
[47] T. Hirano, U.W. Heinz, D. Kharzeev, R. Lacey, and Y. Nara, J. Phys. G **34**, S879 (2007).
[48] B.B. Back *et al.* (PHOBOS Collaboration), Nucl. Phys. **A757**, 28 (2005).
[49] S. Voloshin and A.M. Poskanzer, Phys. Lett. **B474**, 27 (2000).
[50] B. Alver *et al.* (PHOBOS Collaboration), Phys. Rev. Lett. **98**, 242302 (2007).
[51] B.I. Abelev *et al.* (STAR Collaboration), Phys. Rev. C **75**, 054906 (2007).